Continuous Model Applied to Multi-Disk and Multi-Bearing Rotors

Arthur Mereles[a,*], Diogo Stuani Alves[b], Katia Lucchesi Cavalca[a]

[a] *Laboratory of Rotating Machinery, Faculty of Mechanic Engineering, UNICAMP, Rua Mendeleyev, 200, Campinas - SP, Zip code: 13083-860, Brazil*
[b] *Department of Mechanical Engineering, University of Bath, BA2 7AY, Bath, UK.*

Abstract

This work aims at presenting a modeling approach to solve problems in rotordynamics. The method, named Continuous Segment Method (CSM), is valid for systems with several stepped sections and multiple disks and bearings. The shaft is modeled using 1D beam theory, and takes into account gyroscopic effect, rotary inertia and shear deformation. The disks are modeled as concentrated masses with rotary inertia and the bearings can be anisotropic with either long or short characteristics. Long bearings are modeled as elastic foundations whereas short bearings as point-wise spring-damper systems. The basis of the method consist in solving the eigenvalue problem of the system and use the eigenfunctions and eigenvalues to apply modal analysis to discretize the equations of motions. The eigenvalue problem is solved by, firstly, dividing the domain and obtaining local problems. The solution of these, and the use of continuity conditions, allows the obtention of global eigenfunctions and eigenvalues. The evaluation of the CSM is done by comparing its results with the Finite Element Method (FEM) for three applications that are common in rotordynamics: obtention of natural frequencies and mode shapes, response to unbalance and to nonlinear forces. The comparison with the FEM shows that the CSM can be seen as a promising alternative to model complex rotor systems.

Keywords: Multi-stepped rotors; Rotordynamics; Anisotropic bearings; Modal analysis; Continuous system

1. Introduction

Adequate mathematical models are often needed to study physical phenomena, as they help one to form an accurate quantitative representation of the latter. The model provides not only knowledge about the phenomenon itself, but it is also a useful tool to make predictions of the behavior of machines and mechanisms. Thus, the suitability of them to the phenomenon at hand is essential. In rotordynamics, many of the early models were very simple, such as the Jeffcott model, but adequate to explain some phenomena seen in real machinery such as critical speeds and forward and backward whirl. In fact, this model is still used today to study complex rotordynamics effects such as rubbing [1] and cracked rotors [2]. Although the Jeffcott model is a useful approach to rotordynamics, most of the design and study of rotating machines is done by the Finite Element Method (FEM) [3, 4, 5, 6]. The FEM has several options, from 1D to 3D methods, and it offers many advantages, as it can be applied to rotors with complex geometries. The main drawback is the high computational power required, specially for large turbomachines, and in some cases a reduction method is needed [7].

*Corresponding author
Email address: arthur_guilherme_mereles@hotmail.com (Arthur Mereles)

The FEM can be seen as a method to solve a partial differential equation, which are generally the equations of motion of the system [8, 9]. In its most traditional form, the equations are written in the weak form, and the displacement field is interpolated by means of a polynomial function, essentially discretizing the continuous system into a lumped one. Another way to solve the equations of motion is using the separation of variables or the assumed mode method. In these methods, an eigenfunction is obtained from an eigenvalue problem, or it is assumed as having some form. The functions are then used to discretize the continuous system leading to the equations of motion for the modal coordinates. The solutions by the separation of variables are sometimes said to be exact, because no simplification is made in the system, and the equations of motion are solved in their full form. Thus, the solutions using FEM are, in general, approximations of the ones obtained exactly by the separation of variables.

The most general way to model a rotating machine is using 3D models. In such cases, the separation of variables is a rather cumbersome method as compared to the FEM, and is rarely used in the literature. However, a common modeling strategy in rotordynamics is the use of 1D beam models to represent the real machine [10]. In such cases, the bending of the cross section is independent in the two orthogonal directions, but these directions get coupled due to the gyroscopic effect. The application of the separation of variables for beams is relatively easy and well documented [11]. One can also, consider the axial and torsional dynamics by this approach [12, 13, 14]. The bearings can be placed as a spring-damper system and the disks as rigid masses with rotary inertia.

The main weakness of the separation of variables and assumed modes method is their limited applicability, because they might lead to eigenvalue problems which do not always have solutions. In this manner, they are generally applied for systems with uniform geometry and simple boundary conditions. In spite of this, their expansion to complex rotors is readily possible, if the system posses stepped cross sections and lumped masses, as shown in [15, 16, 17, 18, 19, 20]. The basic procedure in this case is: (i) solve the eigenvalue problem for a single shaft segment, (ii) apply continuity or compatibility conditions to relate the functions between segments and (iii) apply the boundary conditions to arrive at the global eigenfunctions and eigenvalues. Nearly all methods proposed apply these, or similar steps, to arrive at a solution using a separation of variables or assumed modes method. Here one can note that, if condition (i) is satisfied, that is, one can solve the problem for each segment, very general rotors can be modeled by this approach.

A problem that arises in rotating systems is the presence of the gyroscopic effect, which makes the eigenvalue problem a non-self-adjoint problem [11]. In such case, the eigenfunctions are not orthogonal, and thus the discretization leads to coupled modal equations. A way to overcome this was shown in [21], where the modal equations were uncoupled by means of an adjoint eigenfunction obtained from the solution of the adjoint eigenvalue problem. In the literature, one does not find much application of modal analysis for continuous gyroscopic systems together with multi-stepped rotors. References [22, 23] show the application of modal analysis for rotors discretized using the FEM. In the case of rotors modeled as continuous systems, most works only consider free-vibration [17], or turn to the frequency domain [19]. Some exceptions are [24, 25, 26], where a method known as component modal expansion is used. With modal analysis, however, the treatment of arbitrary external forces becomes possible, and thus expands the range of application for the rotor model.

This work presents an expansion of previous ones [27, 28], which established the Continuous Segment Method (CSM) for the modeling of rotor systems. In the previous conditions, the bearings were considered only isotropic and

short. The CSM presented here expands the earlier works to account for general anisotropic bearings, with either short or long characteristics. A very distinct approach is taken to solve the equations of motion, which is written using complex coordinates. This makes the interpretation of the response as complex rotating vectors, and it is very suitable for rotating machines [29]. Moreover, a great problem in rotordynamics is the obtention of reduced models to accurately represent the machines. The method proposed in this work can be seen as an alternative to current modeling reduction techniques [30].

The division of the paper is as follows: Section 2 presents the assumptions used to arrive at the equations of motion and the basic problem in rotordynamics. Section 3 shows the CSM, and how it solves the problem stated in the previous section. The results are presented in Sec. 4, and the conclusions in Sec. 5.

2. Problem statement

In rotordynamics, one is mostly concerned with the dynamics of the machines given certain external loads or operation parameters. In order to accomplish that, one generally proposes a mathematical model to represent the phenomena at hand, and, from the results of the model, understand the functioning of the real machine. The dynamics of a great number of mechanical systems can be understood using equations of the form:

$$[m]\{\ddot{w}(x,t)\} + [c]\{\dot{w}(x,t)\} + [k]\{w(x,t)\} = \{f(x,t)\}. \tag{1}$$

Here, $[m]$, $[c]$ and $[k]$ are matrix operators, and represent the mass, damping and/or gyroscopic effects, and stiffness, respectively. The spatial domain x is assumed uni-dimensional, and bounded by the length of the shaft. The vectors $\{w(x,t)\}$ and $\{f(x,t)\}$ are the displacement and external forces fields. To arrive at the specific expression of the terms in Eq. (1), the following assumptions were adopted:

- The shaft is divided into segments, which are modeled as beams; axial and torsional movements are ignored;
- The beam model considers rotary inertia, gyroscopic effects and shear deformation (Timoshenko beam);
- The disks are modeled as concentrated masses with moments of inertia;
- The bearings are modeled as mass-less linear spring-damper systems.

Additionally, the equations are written using a complex notation, which is proven to be effective in the study of rotating machines [22, 31]. Therefore, one has,

$$\{w(x,t)\} = \begin{Bmatrix} w_1(x,t) & w_1^*(x,t) \end{Bmatrix}^T, \quad \{w_1(x,t)\} = \begin{Bmatrix} u(x,t) & \psi(x,t) \end{Bmatrix}^T, \tag{2}$$

$$\{f(x,t)\} = \begin{Bmatrix} g(x,t) & g^*(x,t) \end{Bmatrix}, \quad \{g(x,t)\} = \begin{Bmatrix} f_1(x,t) & 0 \end{Bmatrix}, \tag{3}$$

$$[m] = \begin{bmatrix} \bar{m}(x) & 0 & 0 & 0 \\ 0 & \bar{J}_d(x) & 0 & 0 \\ 0 & 0 & \bar{m}(x) & 0 \\ 0 & 0 & 0 & \bar{J}_d(x) \end{bmatrix} \tag{4}$$

,

$$[c] = \begin{bmatrix} [c_1] & [c_2] \\ [c_2^*] & [c_1^*] \end{bmatrix}, \quad [c_1] = \begin{bmatrix} \bar{c}_f(x) & 0 \\ 0 & -j\Omega \bar{J}_p(x) \end{bmatrix}, \quad [c_2] = \begin{bmatrix} \bar{c}_b(x) & 0 \\ 0 & 0 \end{bmatrix}, \tag{5}$$

$$[k] = \begin{bmatrix} [k_1] & [k_2] \\ [k_2^*] & [k_1^*] \end{bmatrix}, \quad [k_1] = \begin{bmatrix} -\dfrac{\partial}{\partial x}\left(\kappa G\bar{A}(x)\dfrac{\partial}{\partial x}\right) + \bar{k}_f(x) & \dfrac{\partial}{\partial x}\left(\kappa G\bar{A}(x)\right) \\ -\kappa G\bar{A}(x)\dfrac{\partial}{\partial x} & -\dfrac{\partial}{\partial x}\left(E\bar{I}(x)\dfrac{\partial}{\partial x}\right) + \kappa G\bar{A}(x) \end{bmatrix},$$

$$[k_2] = \begin{bmatrix} \bar{k}_b(x) & 0 \\ 0 & 0 \end{bmatrix}, \tag{6}$$

where * denotes the complex conjugate, $u(x,t)$ and $\psi(x,t)$ are the complex displacement and rotation fields along the length of the shaft; $f_1(x,t)$ is the external distributed force; $\bar{m}(x)$, $\bar{J}_d(x)$ and $\bar{J}_p(x)$ are the mass, diametral and polar moments of inertia per unit length, respectively; $\bar{A}(x)$ is the cross sectional area; $\bar{I}(x)$ the second moment of area; G, E, ρ, and κ are the shear modulus, Young's modulus, density and shear correction factor, respectively. These parameters are distributed in a step-wise manner, that is, they are constant for each segment of the shaft. By using the expressions of the matrices listed above, one can obtain the complex equations of motion.

The parameters of the bearings are encoded in the functions $\bar{k}_b(x)$, $\bar{k}_f(x)$, $\bar{c}_b(x)$ and $\bar{c}_f(x)$, which are given as,

$$\begin{aligned} \bar{k}_f(x) &= \frac{1}{2}\Big(k_{yy}(x) + k_{zz}(x) - j(k_{yz}(x) - k_{zy}(x))\Big), \\ \bar{c}_f(x) &= \frac{1}{2}\Big(c_{yy}(x) + c_{zz}(x) - j(c_{yz}(x) - c_{zy}(x))\Big), \\ \bar{k}_b(x) &= \frac{1}{2}\Big(k_{yy}(x) - k_{zz}(x) + j(k_{yz}(x) + k_{zy}(x))\Big), \\ \bar{c}_b(x) &= \frac{1}{2}\Big(c_{yy}(x) - c_{zz}(x) + j(c_{yz}(x) + c_{zy}(x))\Big), \end{aligned} \tag{7}$$

where the subscripts yy and zz denote the direct coefficients, while the remaining ones the cross-coupled coefficients. The form presented in Eq. (7) allows the modeling of a large number of bearings used in rotating machines [32, 33]. In case one has isotropic bearings, it follows that $\bar{k}_b(x) = \bar{c}_b(x) = 0$. The result of this is the decoupling of the displacements and their complex conjugates in the equations of motion; thus, they need not to be solved simultaneously. Note, however, that for general anisotropic bearings, this is not the case.

To solve Eq. (1), given the matrices and vectors listed in Eqs. (2)-(6), one firstly write it in a state-space form,

$$[M]\{\dot{W}(x,t)\} = [K]\{W(x,t)\} + \{F(x,t)\}, \tag{8}$$

where,

$$\{W(x,t)\} = \Big\{\{\dot{w}(x,t)\}\ \{w(x,t)\}\Big\}^T, \tag{9}$$

$$\{F(x,t)\} = \Big\{0\ \{f(x,t)\}\Big\}^T, \tag{10}$$

$$[M] = \begin{bmatrix} [0]_{2\times 2} & [m] \\ [m] & [c] \end{bmatrix}, \tag{11}$$

$$[K] = \begin{bmatrix} [m] & [0]_{2\times 2} \\ [0]_{2\times 2} & -[k] \end{bmatrix}, \tag{12}$$

Next, one may assume a solution on the form,

$$\{W(x,t)\} = \sum_{i=1}^{\infty} \{\Phi_i(x)\} q_i(t), \tag{13}$$

being $\{\Phi_i(x)\}$ a vector with the the ith vibration modes or eigenfunctions and $q_i(t)$ the ith modal or generalized coordinates. The method above is also known as a time-space separation procedure [34]. Upon substituting the assumed solution in Eq. (8), one has,

$$\sum_{i=1}^{\infty} [M]\{\Phi_i(x)\}\dot{q}_i(t) = \sum_{i=1}^{\infty} [K]\{\Phi_i(x)\} q_i(t) + \{F(x,t)\}. \tag{14}$$

In order to solve the above equation, one needs to perform a discretization procedure. One way of doing that, is to take the internal product of it with a test function $\{\tilde{\Phi}_i(x)\}$. This is essentially a projection of the equation of motion in the space of functions $\left[\{\tilde{\Phi}_i(x)\}\right]_{i=1}^{\infty}$. The solution of Eq. (14) will be much easier if the projection leads to uncoupled equations for the generalized coordinates q_i. This can be done by ensuring that $\{\Phi_i(x)\}$ and $\{\tilde{\Phi}_i(x)\}$ satisfy the following conditions:

$$\langle\, [M]\{\Phi_i(x)\},\, \{\tilde{\Phi}_j(x)\}\,\rangle = \delta_{ij}, \tag{15a}$$

$$\langle\, [K]\{\Phi_i(x)\},\, \{\tilde{\Phi}_j(x)\}\,\rangle = \lambda_i \delta_{ij}, \tag{15b}$$

where δ_{ij} is the Kronecker delta, which is one if $i = j$ and zero if $i \neq j$; λ_i is the eigenvalue, and the operator $\langle\cdot\rangle$ denotes the internal product [11]. Note that the orthogonality conditions as given in Eqs. (15a) and (15b), imply a normalization of the vectors $\{\Phi_i(x)\}$ and $\{\tilde{\Phi}_i(x)\}$. By applying the internal product in Eq. (14) with $\{\tilde{\Phi}_j(x)\}$, and taking into account the orthogonality conditions above, one finds,

$$\dot{q}_i(t) = \lambda_i q_i(t) + \langle\, \{F(x,t)\},\, \{\tilde{\Phi}_i(x)\}\,\rangle \quad \text{for} \quad i = 1, 2, \ldots \quad . \tag{16}$$

Equation (16) consist of an infinite number of first-order differential equations, which solution gives the generalized coordinates $q_i(t)$ given an external force $\{F(x,t)\}$. The main difficulty in the above approach is the obtention of the eigenfunctions $\{\Phi_i(x)\}$ and test function $\{\tilde{\Phi}_i(x)\}$. They must be found by solving the following eigenvalue problems [29, 35],

$$\lambda[M]\{\Phi(x)\} = [K]\{\Phi(x)\}, \tag{17}$$

$$\lambda^*[\tilde{M}]\{\tilde{\Phi}(x)\} = [\tilde{K}]\{\tilde{\Phi}(x)\}, \tag{18}$$

where $[\tilde{M}] = [M]^H$ and $[\tilde{K}] = [K]^H$, being H the hermitian or complex conjugate transpose. Equation (17) is derived from the equation of motion and (18) from the orthogonality conditions. The problems above are also subjected to the boundary conditions of the rotor in both ends. The application of the boundary conditions will be shown later.

With $\{\Phi_i(x)\}$ and $q_i(t)$ at hand, one can obtain the displacement field from Eq. (13). The next section presents a method for the solution of the problem stated above.

Before moving on to the proposed method, it is worth mentioning alternatives that could have been adopted to solve the same problem. The main method used in the literature is the FEM. Given the above formulation, the FEM would differ in the assumed solution, Eq. (13), where the vector $\{\Phi_i(x)\}$ would be a polynomial and $q_i(t)$ would represent the physical displacements and rotations at certain locations of the shaft [32]. Since the form of $\{\Phi_i(x)\}$ is assumed, one does not need to solve an eigenvalue problem. Such functions are known in the literature as comparison functions [11]. Another approach is to adopt a simplified form for the matrices $[M]$ and $[K]$ in Eq. (17), making the obtention of the eigenfunctions easier, and assuming $\{\tilde{\Phi}_i(x)\} = \{\Phi_i(x)\}$. This method is known as assumed modes method [36], and the functions obtained from such methods are often called admissible functions [11]. These alternative methods can be seen as an approximate solution to the equations of motion. By adopting the approach presented in this paper, one arrives at the exact solutions, given, of course, the assumptions adopted.

3. Continuous segment method

This section presents the CSM, that aims at solving the problem previously stated. Firstly, the system is divided as shown in Fig. 1. Here one has a stepped and homogeneous shaft with n segments, each with constant cross section. Each segment has a local coordinate ξ_i, bounded by $[0,\ L_i]$, being L_i the length of the segment and $i = 1, 2, .., n$. On the segments, one can have a disk or a bearing, and their local coordinates are denoted by a and b, as illustrated in the figure. The coordinate system and the direction of the displacements are also shown in the depiction, and the relation between them and the complex displacements are $u(x,t) = u_y(x,t) + ju_z(x,t)$ and $\psi(x,t) = \psi_z(x,t) - j\psi_y(x,t)$, where j is the imaginary number.

The eigenvalue problem as presented in Eq. (17) cannot be solved, since the coefficients of the resulting differential equations are not constant. However, one can write this problem for each segment separately. This allows the solution to be obtained for each individual segment; the global solution will come from the application of continuity

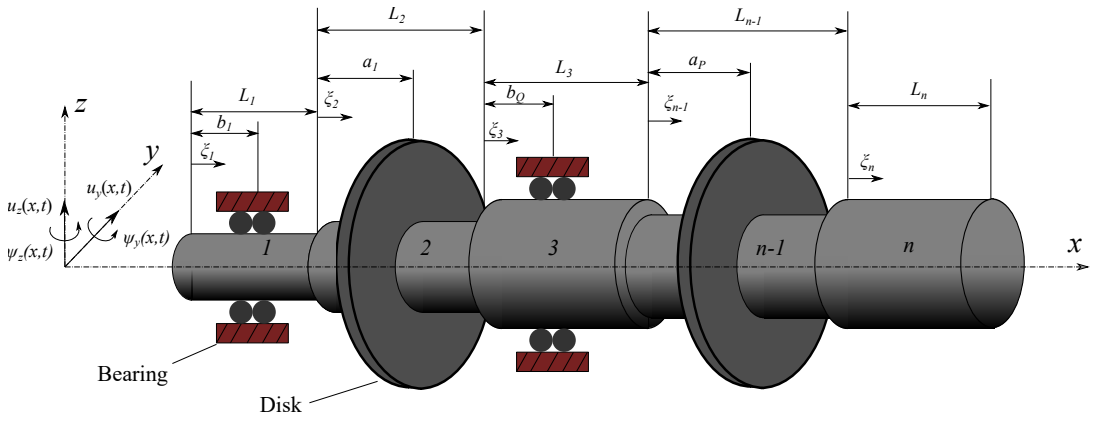

Figure 1: Depiction of the system studied.

or compatibility conditions. The vector of mode shapes can be written for local segments as,

$$\{\Phi^i(\xi_i)\} = \Big\{\lambda\{\phi^i(\xi_i)\} \quad \{\phi^i(\xi_i)\}\Big\}^T, \tag{19}$$

with,

$$\{\phi^i(\xi_i)\} = \Big\{\phi_1^i(\xi_i) \quad \eta_1^i(\xi_i) \quad \phi_2^i(\xi_i) \quad \eta_2^i(\xi_i)\Big\}^T. \tag{20}$$

Here, the superscript i denotes the ith segment, and the functions ϕ_1, ϕ_2, η_1 and η_2 are eigenfunctions to be found. Using the above definition for $\{\Phi^i(\xi_i)\}$, Eq. (17) can be expressed as,

$$\lambda[m^i]\{\phi^i(\xi_i)\} = \lambda[m^i]\{\phi^i(\xi_i)\} \tag{21a}$$

$$\Big(\lambda^2[m^i] + \lambda[c^i] + [k^i]\Big)\{\phi^i(\xi_i)\} = 0 \tag{21b}$$

The trivial equation (21a) arises due to the state-space formulation. The local matrices can be written as,

$$[m^i] = \begin{bmatrix} \rho A_i + M^k\delta_d(\xi_i - a_k) & 0 & 0 & 0 \\ 0 & \rho A_i r_i^2 + J_d^k\delta_d(\xi_i - a_k) & 0 & 0 \\ 0 & 0 & \rho A_i + M^k\delta_d(\xi_i - a_k) & 0 \\ 0 & 0 & 0 & \rho A_i r_i^2 + J_d^k\delta_d(\xi_i - a_k) \end{bmatrix} \tag{22}$$

,

$$[c^i] = \begin{bmatrix} [c_1] & [c_2] \\ [c_2^*] & [c_1^*] \end{bmatrix}, \quad [c_1] = \begin{bmatrix} \bar{c}_f(\xi_i) & 0 \\ 0 & -j\Omega\Big(2\rho A_i r_i^2 + J_p^k\delta_d(\xi_i - a_k)\Big) \end{bmatrix}, \quad [c_2] = \begin{bmatrix} \bar{c}_b(\xi_i) & 0 \\ 0 & 0 \end{bmatrix}, \tag{23}$$

$$[k^i] = \begin{bmatrix} [k_1] & [k_2] \\ [k_2^*] & [k_1^*] \end{bmatrix}, \quad [k_1] = \begin{bmatrix} -\kappa G A_i\dfrac{\partial^2}{\partial x^2} + \bar{k}_f(\xi_i) & \kappa G A_i\dfrac{\partial}{\partial x} \\ -\kappa G A_i\dfrac{\partial}{\partial x} & -EI_i\dfrac{\partial^2}{\partial x^2} + \kappa G A_i \end{bmatrix},$$

$$[k_2] = \begin{bmatrix} \bar{k}_b(\xi_i) & 0 \\ 0 & 0 \end{bmatrix}. \tag{24}$$

The properties of the shaft for segment i are the cross-sectional areal A_i, area moment of inertia I_i, and radius of gyration r_i; M^k, J_d^k and J_p^k are the mass, diametral and polar moments of inertia of the kth disk; and δ_d is the Dirac's delta function. In addition, the local functions of the bearings depend if they are modeled as long or short:

- Short bearings

$$\bar{k}_f(\xi_i) = k_f^l\delta_d(\xi_i - b_l),\ \bar{k}_b(\xi_i) = k_b^l\delta_d(\xi_i - b_l),\ \bar{c}_f(\xi_i) = c_f^l\delta_d(\xi_i - b_l),\ \bar{c}_b(\xi_i) = c_b^l\delta_d(\xi_i - b_l) \tag{25a}$$

- Long bearings

$$\bar{k}_f(\xi_i) = k_f^l,\ \bar{k}_b(\xi_i) = k_b^l,\ \bar{c}_f(\xi_i) = c_f^l,\ \bar{c}_b(\xi_i) = c_b^l \tag{25b}$$

where l denotes the lth bearing and b_l is the local coordinate of the bearing (see Fig. 1). Short bearings are modeled as a massless spring-damper system positioned at a single point on the shaft. This approach is suitable for rotors with fluid-film bearings with low length-to-diameter ratio ($L : D < 1$), or with rolling-element bearings. Long bearings

are modeled as a distributed stiffness along the shaft, similar to an elastic foundation. For simplicity, the distributed stiffness is considered acting on the whole segment instead of only on part of it. Thus, the length of the bearing can be adjusted by changing the length of the segment. This approach is suited to rotors with fluid-film bearings that posses high length-to-diameter ratio, or any other type of bearing that has a clamped-like effect in the shaft.

A further expansion of Eq. (21b) leads to,

$$\begin{aligned}\lambda^2\Big(\rho A_i + M^k\delta_d(\xi_i - a_k)\Big)\phi_1^i(\xi_i) + \kappa G A_i\Big(\eta_1^{i\prime}(\xi_i) - \phi_1^{i\prime\prime}(\xi_i)\Big)\\ + \left[\bar{k}_f(\xi_i) + \lambda\bar{c}_f(\xi_i)\right]\phi_1^i(\xi_i) + \left[\bar{k}_b(\xi_i) + \lambda\bar{c}_b(\xi_i)\right]\phi_2^i(\xi_i) = 0,\end{aligned} \tag{26a}$$

$$\begin{aligned}\lambda^2\Big(\rho A_i + M^k\delta_d(\xi_i - a_k)\Big)\phi_2^i(\xi_i) + \kappa G A_i\Big(\eta_2^{i\prime}(\xi_i) - \phi_2^{i\prime\prime}(\xi_i)\Big)\\ + \left[\bar{k}_f^*(\xi_i) + \lambda\bar{c}_f^*(\xi_i)\right]\phi_2^i(\xi_i) + \left[\bar{k}_b^*(\xi_i) + \lambda\bar{c}_b^*(\xi_i)\right]\phi_1^i(\xi_i) = 0,\end{aligned} \tag{26b}$$

$$\begin{aligned}\lambda^2\Big(\rho A_i r_i^2 + J_d^k\delta_d(\xi_i - a_k)\Big)\eta_1^i(\xi_i) - j\lambda\Omega\Big(2\rho A_i r_i^2 + J_p^k\delta_d(\xi_i - a_k)\Big)\eta_1^i(\xi_i)\\ - EI_i\eta_1^{i\prime\prime}(\xi_i) + \kappa G A_i\Big(\eta_1^i(\xi_i) - \phi_1^{i\prime}(\xi_i)\Big) = 0,\end{aligned} \tag{26c}$$

$$\begin{aligned}\lambda^2\Big(\rho A_i r_i^2 + J_d^k\delta_d(\xi_i - a_k)\Big)\eta_2^i(\xi_i) + j\lambda\Omega\Big(2\rho A_i r_i^2 + J_p^k\delta_d(\xi_i - a_k)\Big)\eta_2^i(\xi_i)\\ - EI_i\eta_2^{i\prime\prime}(\xi_i) + \kappa G A_i\Big(\eta_2^i(\xi_i) - \phi_2^{i\prime}(\xi_i)\Big) = 0.\end{aligned} \tag{26d}$$

Here, the prime denotes differentiation with respect to ξ_i, that is, $' = d/d\xi_i$. An important fact from the above equations is that, the first and second (or third and forth) are not complex conjugate equations only due to the anisotropic bearing coefficients $\bar{k}_b$ and $\bar{c}_b$. Thus, when one has $\bar{k}_b = \bar{c}_b = 0$, only one pair of the equations needs to be solved. This was done in the isotropic case treated in [27, 28]. For general anisotropic bearings, the four equations need to be solved simultaneously. In addition, one may also notice that the direction of rotation (Ω) is not the same for the equations. This implies that the functions ϕ_1 and η_1 rotate in the opposite direction of ϕ_2 and η_2.

The solution of Eq. (21b) or (26a)-(26d) can be obtained through the Laplace transform, which gives,

$$[L]\{\hat{\Phi}^i(s)\} = \{b\}, \tag{27}$$

where,

$$\{\hat{\Phi}^i(s)\} = \begin{Bmatrix}\hat{\phi}_1^i(s) & \hat{\eta}_1^i(s) & \hat{\phi}_2^i(s) & \hat{\eta}_2^i(s)\end{Bmatrix}^T, \tag{28}$$

being s the spatial coordinate in the s-domain, and the hat symbol in $\hat{\phi}_1^i(s)$, denotes the Laplace transform of the function $\phi_1^i(\xi_i)$, and similarly to the other quantities. The matrix $[L]$ and the vector $\{b\}$ will be different for short and long bearings:

- Short bearing

$$[L] = \begin{bmatrix}[L_1] & [0]_{4\times4}\\ [0]_{4\times4} & [L_2]\end{bmatrix}, \quad [L_1] = \begin{bmatrix}\rho A_i\lambda^2 - \kappa G A_i s^2 & \kappa G A_i s\\ -\kappa G A_i s & \left(\lambda^2 - 2j\lambda\Omega\right)\rho A_i r_i^2 - EI_i s^2 + \kappa G A_i\end{bmatrix},$$

$$[L_2] = \begin{bmatrix}\rho A_i\lambda^2 - \kappa G A_i s^2 & \kappa G A_i s\\ -\kappa G A_i s & \left(\lambda^2 + 2j\lambda\Omega\right)\rho A_i r_i^2 - EI_i s^2 + \kappa G A_i\end{bmatrix} \tag{29a}$$

$$\{b\} = \begin{Bmatrix} \kappa GA_i \left[\eta_i(0) - \phi_i'(0) - s\phi(0)\right] - \lambda^2 M^k \phi_i(a_k) e^{-sa_k} \\ -\Big(\left(k_f^l + \lambda c_f^l\right) \phi_{1i}(b_l) + \left(k_b^l + \lambda c_b^l\right) \phi_{2i}(b_l) \Big) e^{-sb_l} \\ \\ -\kappa GA_i \phi_i(0) - EI_i \left[\eta_i'(0) + s\eta_i(0)\right] - \left(\lambda^2 J_d^k - j\lambda\Omega J_p^k\right) \eta_i(a_k) e^{-sa_k} \\ + \left(k_t^l + \lambda c_t^l\right) \eta_i(b_l) e^{-sb_l} \\ \\ \kappa GA_i \left[\eta_i(0) - \phi_i'(0) - s\phi(0)\right] - \lambda^2 M^k \phi_i(a_k) e^{-sa_k} \\ -\Big(\left(k_f^{l*} + \lambda c_f^{l*}\right) \phi_{2i}(b_l) + \left(k_b^{l*} + \lambda c_b^{l*}\right) \phi_{1i}(b_l) \Big) e^{-sb_l} \\ \\ -\kappa GA_i \phi_i(0) - EI_i \left[\eta_i'(0) + s\eta_i(0)\right] - \left(\lambda^2 J_d^k + j\lambda\Omega J_p^k\right) \eta_i(a_k) e^{-sa_k} \\ + \left(k_t^l + \lambda c_t^l\right) \eta_i(b_l) e^{-sb_l} \end{Bmatrix} \tag{29b}$$

- Long Bearing

$$[L] = \begin{bmatrix} [L_1] & [L_2] \\ [L_3] & [L_4] \end{bmatrix}, \quad [L_1] = \begin{bmatrix} \rho A_i \lambda^2 - \kappa GA_i s^2 + \left(k_f^l + \lambda c_f^l\right) & \kappa GA_i s \\ -\kappa GA_i s & \left(\lambda^2 - 2j\lambda\Omega\right) \rho A_i r_i^2 - EI_i s^2 + \kappa GA_i \end{bmatrix},$$

$$[L_2] = \begin{bmatrix} \left(k_b^l + \lambda c_b^l\right) & 0 \\ 0 & 0 \end{bmatrix}, \quad [L_3] = \begin{bmatrix} \left(k_b^{l*} + \lambda c_b^{l*}\right) & 0 \\ 0 & 0 \end{bmatrix}$$

$$[L_4] = \begin{bmatrix} \rho A_i \lambda^2 - \kappa GA_i s^2 + \left(k_f^{l*} + \lambda c_f^{l*}\right) & \kappa GA_i s \\ -\kappa GA_i s & \left(\lambda^2 + 2j\lambda\Omega\right) \rho A_i r_i^2 - EI_i s^2 + \kappa GA_i \end{bmatrix} \tag{30a}$$

$$\{b\} = \begin{Bmatrix} \kappa GA_i \left[\eta_i(0) - \phi_i'(0) - s\phi(0)\right] - \lambda^2 M^k \phi_i(a_k) e^{-sa_k} \\ \\ -\kappa GA_i \phi_i(0) - EI_i \left[\eta_i'(0) + s\eta_i(0)\right] - \left(\lambda^2 J_d^k - j\lambda\Omega J_p^k\right) \eta_i(a_k) e^{-sa_k} \\ \\ \kappa GA_i \left[\eta_i(0) - \phi_i'(0) - s\phi(0)\right] - \lambda^2 M^k \phi_i(a_k) e^{-sa_k} \\ \\ -\kappa GA_i \phi_i(0) - EI_i \left[\eta_i'(0) + s\eta_i(0)\right] - \left(\lambda^2 J_d^k + j\lambda\Omega J_p^k\right) \eta_i(a_k) e^{-sa_k} \end{Bmatrix} \tag{30b}$$

One can note that the problem for short and long bearings are very similar. The main difference is that, due to the use of the Dirac delta, the bearing coefficients for the short bearing land on the vector $\{b\}$. This makes the matrix $[L]$ block diagonal, essentially decoupling the equations for $\hat{\phi}_{1i}(s)$ and $\hat{\eta}_{1i}(s)$ with $\hat{\phi}_{2i}(s)$ and $\hat{\eta}_{2i}(s)$. On the other hand, for long bearings, the coefficients are in the matrix $[L]$, coupling the four equations.

In order to obtain the functions in the space domain, the Inverse Laplace Transform must be applied in Eq. (27). Firstly, the equation must be solved for $\{\hat{\Phi}(s)\}$, which will require the inversion of the matrix $[L]$. Recalling that the inverse of a matrix can be given as $[L]^{-1} = adj([L])/det([L])$, where adj denotes the adjugate matrix and det the determinant. Thus, Eq. (27) can be written as:

$$\{\hat{\Phi}^i(s)\} = \frac{adj([L])}{det([L])}\{b\} = det([L])^{-1}\{\bar{b}\} \tag{31}$$

where $\{\bar{b}\} = adj([L])\{b\}$. The determinant of the matrix $[L]$ will be a polynomial function, and can be written as,

$$det([L]) = (s^2 - \epsilon_{1i}^2)(s^2 - \epsilon_{2i}^2)(s^2 - \epsilon_{3i}^2)(s^2 - \epsilon_{4i}^2) \tag{32}$$

being ϵ_{ji} $(j = 1, 2, 3, 4)$ the roots of the equation $det([L]) = 0$. These roots are the mode shape parameters, also known as wave numbers. With the roots ϵ_{ji} $(j = 1, 2, 3, 4)$ at hand, the Inverse Laplace Transform can be applied in Eq. (31). The functions of segment i in the space domain will have the following general form,

$$\phi_1^i(\xi_i) = [C^i(\xi_i)]\{X^i(0)\}, \tag{33}$$

$$\eta_1^i(\xi_i) = [D^i(\xi_i)]\{X^i(0)\}, \tag{34}$$

$$\phi_2^i(\xi_i) = [E^i(\xi_i)]\{X^i(0)\}, \tag{35}$$

$$\eta_2^i(\xi_i) = [F^i(\xi_i)]\{X^i(0)\}, \tag{36}$$

where,

$$[C^i(\xi)] = [C_1^i(\xi)\ C_2^i(\xi)\ \cdots\ C_8^i(\xi)], \quad [D^i(\xi)] = [D_1^i(\xi)\ D_2^i(\xi)\ \cdots\ D_8^i(\xi)], \tag{37}$$

$$[E^i(\xi)] = [E_1^i(\xi)\ E_2^i(\xi)\ \cdots\ E_8^i(\xi)], \quad [F^i(\xi)] = [F_1^i(\xi)\ F_2^i(\xi)\ \cdots\ F_8^i(\xi)], \tag{38}$$

$$\{X^i(\xi_i)\} = \{\eta_1^i(\xi_i)\ \eta_1^{i\prime}(\xi_i)\ \phi_1^i(\xi_i)\ \phi_1^{i\prime}(\xi_i)\ \eta_2^i(\xi_i)\ \eta_2^{i\prime}(\xi_i)\ \phi_2^i(\xi_i)\ \phi_2^{i\prime}(\xi_i)\}^T. \tag{39}$$

The functions C_{ji}, D_{ji}, E_{ji} and F_{ji} $(j = 1, 2, ..., 8)$ posses the information about the shaft's properties and if the segment i has a disk or a bearing. Appendix A lists their full form.

Equations (33)-(36) are the solutions of the local eigenvalue problem, Equation (21). However, one still needs to find the constants $\{X^i(0)\}$, which are obtained through the application of boundary conditions. The next step is to find a way to relate these functions, which are local for each segments, and obtain the global modes that are used in the expansion (13). This can be done by means of the continuity conditions, which are the continuity of the displacement, rotation, shearing force and bending moment across the segments. These conditions can be written as,

$$\begin{cases} u^i(\xi_i = L_i, t) = u^{i+1}(\xi_{i+1} = 0, t) \\ \psi^i(\xi_i = L_i, t) = \psi^{i+1}(\xi_{i+1} = 0, t) \\ EI_i \dfrac{\partial \psi^i(\xi_i = L_i, t)}{\partial \xi_i} = EI_{i+1} \dfrac{\partial \psi^{i+1}(\xi_{i+1} = 0, t)}{\partial \xi_{i+1}} \\ \kappa G A_i \left(\psi^i(\xi_i = L_i, t) - \dfrac{\partial u^i(\xi_i = L_i, t)}{\partial \xi_i} \right) = \kappa G A_{i+1} \left(\psi^{i+1}(\xi_{i+1} = 0, t) - \dfrac{\partial u^{i+1}(\xi_{i+1} = 0, t)}{\partial \xi_{i+1}} \right) \end{cases} \tag{40}$$

Here u^i and ψ^i are the displacement and slope in local coordinates of segment i. Note that the conditions do not consider bearings or disks on the boundaries. By using the assumed solution shown in Eq. (13), together with Eq. (19),

in the conditions above, one arrives at,

$$\begin{cases} \phi_1^{i+1}(0) = \phi_1^i(L_i) \\ \phi_2^{i+1}(0) = \phi_2^i(L_i) \\ \eta_1^{i+1}(0) = \eta_1^i(L_i) \\ \eta_2^{i+1}(0) = \eta_2^i(L_i) \\ EI_{i+1}\eta_1^{i+1\prime}(0) = EI_i\eta_1^{i\prime}(L_i) \\ EI_{i+1}\eta_2^{i+1\prime}(0) = EI_i\eta_2^{i\prime}(L_i) \\ \kappa GA_{i+1}\Big(\eta_1^{i+1}(0) - \phi_1^{i+1\prime}(0)\Big) = \kappa GA_i\Big(\eta_1^i(L_i) - \phi_1^{i\prime}(L_i)\Big) \\ \kappa GA_{i+1}\Big(\eta_2^{i+1}(0) - \phi_2^{i+1\prime}(0)\Big) = \kappa GA_i\Big(\eta_2^i(L_i) - \phi_2^{i\prime}(L_i)\Big) \end{cases} \tag{41}$$

It's worth mentioning that the continuity conditions for ϕ_1^i and η_1^i, as shown above, are uncoupled from ϕ_2^i and η_2^i due to the symmetry of the shaft properties. For asymmetric shafts, for example, this will not be the case. Writing in matrix form, Eq. (41) can be stated as:

$$\{X_{i+1}(0)\} = [H_{1i}]\{X_i(L_i)\}, \tag{42}$$

being,

$$[H_{1i}] = \begin{bmatrix} [h_i] & [0]_{4\times4} \\ [0]_{4\times4} & [h_i] \end{bmatrix}, \quad [h_i] = \begin{bmatrix} 1 & 0 & 0 & 0 \\ 0 & \beta_i & 0 & 0 \\ 0 & 0 & 1 & 0 \\ 1-\alpha_i & 0 & 0 & \alpha_i \end{bmatrix}, \tag{43}$$

and $\beta_i = I_i/I_{i+1}$, $\alpha_i = A_i/A_{i+1}$ and $[0]_{4\times4}$ is a 4×4 matrix with zeros. The matrix $[h_i]$ is taken directly from Eq. (41), and it takes into account the change in the geometry between segments. In case there is no change in the geometry, the matrix becomes simply the identity matrix. By utilizing the relations shown in Eqs. (33)-(36), one has,

$$\begin{aligned} \{X_i(L_i)\} &= \begin{Bmatrix} \eta_{1i}(L_i) \\ \eta'_{1i}(L_i) \\ \phi_{1i}(L_i) \\ \phi'_{1i}(L_i) \\ \vdots \\ \phi'_{2i}(L_i) \end{Bmatrix} = \begin{Bmatrix} [D_i(L_i)]\{X_i(0)\} \\ [D'_i(L_i)]\{X_i(0)\} \\ [C_i(L_i)]\{X_i(0)\} \\ [C'_i(L_i)]\{X_i(0)\} \\ \vdots \\ [F'_i(L_i)]\{X_i(0)\} \end{Bmatrix} = \\ &= \Big[[D_i(L_i)] \quad [D'_i(L_i)] \quad \cdots \quad [F'_i(L_i)]\Big]^T \{X_i(0)\}. \end{aligned} \tag{44}$$

Therefore, Equation (42) can be written as

$$\{X_{i+1}(0)\} = [H_{1i}]\Big[[D_i(L_i)] \quad [D'_i(L_i)] \quad \cdots \quad [F'_i(L_i)]\Big]^T \{X_i(0)\} = [H_i]\{X_i(0)\}. \tag{45}$$

Equation (45) essentially relates the unknowns parameters of segment i with $i+1$ through a transfer matrix $[H_i]$, which contains the properties of the geometry of the shaft as well as any disks or bearings contained in the segments. This equation can also be used to relate the eigenfunctions of the different segments.

The last step, requires the application of the boundary conditions, so that unique eigenfunctions and eigenvalues are obtained. Here, only simple boundary conditions are considered, such as free-free, simply-supported or clamped. Consider a shaft that is free at both ends. The conditions are shear force and bending moments zero at these locations, thus,

$$\begin{cases} EI_1 \dfrac{\partial \psi^1(\xi_1 = 0, t)}{\partial \xi_1} = 0 \\ EI_n \dfrac{\partial \psi^n(\xi_n = L_n, t)}{\partial \xi_n} = 0 \\ \kappa G A_1 \left(\psi^1(\xi_1 = 0, t) - \dfrac{\partial u^1(\xi_1 = 0, t)}{\partial \xi_1} \right) = 0 \\ \kappa G A_n \left(\psi^n(\xi_n = L_n, t) - \dfrac{\partial u^n(\xi_n = L_n, t)}{\partial \xi_n} \right) = 0 \end{cases} \tag{46}$$

Through Eqs. (13) and (19), the above conditions can be written simply as,

$$\begin{cases} \eta_1^{1\prime}(0) = \eta_2^{1\prime}(0) = \eta_1^{n\prime}(L_n) = \eta_2^{n\prime}(L_n) = 0 \\ \kappa G A_1 \Big(\eta_1^1(0) - \phi_1^1(0) \Big) = \kappa G A_1 \Big(\eta_2^1(0) - \phi_2^1(0) \Big) = 0 \\ \kappa G A_n \Big(\eta_1^n(L_n) - \phi_1^n(L_n) \Big) = \kappa G A_n \Big(\eta_2^n(L_n) - \phi_2^n(L_n) \Big) = 0 \end{cases} \tag{47}$$

Next, one can use Eq. (45), to write the functions of segment n as:

$$\phi_1^n(\xi_n) = [C_n(\xi_n)]\{X_n(0)\} = [C_n(\xi_n)]\Big([H_{n-1}] \times [H_{n-2}] \times \cdots \times [H_1]\Big)\{X_1(0)\}$$

$$\eta_1^n(\xi_n) = [D_n(\xi_n)]\{X_n(0)\} = [D_n(\xi_n)]\Big([H_{n-1}] \times [H_{n-2}] \times \cdots \times [H_1]\Big)\{X_1(0)\}$$

$$\phi_2^n(\xi_n) = [E_n(\xi_n)]\{X_n(0)\} = [E_n(\xi_n)]\Big([H_{n-1}] \times [H_{n-2}] \times \cdots \times [H_1]\Big)\{X_1(0)\}$$

$$\eta_2^n(\xi_n) = [F_n(\xi_n)]\{X_n(0)\} = [F_n(\xi_n)]\Big([H_{n-1}] \times [H_{n-2}] \times \cdots \times [H_1]\Big)\{X_1(0)\}$$

By utilizing the above equations in (47), and writing the system of equations in matrix form, the following is obtained,

$$\begin{bmatrix} [D_n'(L_n)] \\ [D_n(L_n)] - [C_n'(L_n)] \\ [F_n'(L_n)] \\ [F_n(L_n)] - [E_n'(L_n)] \end{bmatrix} \Big([H_{n-1}] \times [H_{n-2}] \times \cdots \times [H_1]\Big)\{X_1(0)\} = 0 \tag{48}$$

Lastly, one needs to apply the boundary conditions at $x = 0$ in the above equation by altering the term $[H_1]\{X_1(0)\}$. This can be done as,

$$[H_1]\{X_1(0)\} = [H_1] \begin{Bmatrix} \eta_1^1(0) \\ \eta_1^{1\prime}(0) \\ \phi_1^1(0) \\ \phi_1^{1\prime}(0) \\ \eta_2^1(0) \\ \eta_2^{1\prime}(0) \\ \phi_2^1(0) \\ \phi_2^{1\prime}(0) \end{Bmatrix} = [H_1] \begin{Bmatrix} \phi_1^{1\prime}(0) \\ 0 \\ \phi_1^1(0) \\ \phi_1^{1\prime}(0) \\ \phi_2^{1\prime}(0) \\ 0 \\ \phi_2^1(0) \\ \phi_2^{1\prime}(0) \end{Bmatrix} = [H_1] \begin{bmatrix} 0 & 1 & 0 & 0 \\ 0 & 0 & 0 & 0 \\ 1 & 0 & 0 & 0 \\ 0 & 1 & 0 & 0 \\ 0 & 0 & 0 & 1 \\ 0 & 0 & 0 & 0 \\ 0 & 0 & 1 & 0 \\ 0 & 0 & 0 & 1 \end{bmatrix} \begin{Bmatrix} \phi_1^1(0) \\ \phi_1^{1\prime}(0) \\ \phi_2^1(0) \\ \phi_2^{1\prime}(0) \end{Bmatrix} = [B]\{X\}$$

Substituting the above expression in the previous one, one arrives at,

$$[A]\Big([H_{n-1}]\times[H_{n-2}]\times\cdots\times[H_2]\Big)[B]\{X\}=[G(\lambda)]\{X\}=0. \tag{49}$$

Note that, for different boundary conditions, one needs to change only the matrices $[A]$ and $[B]$, and the vector of unknowns $\{X\}$. From the approach outlined, the expansion for the simply-supported and clamped boundary conditions is straightforward. Equation (49) can be identified as the system of equations to obtain the relative amplitudes between the vibration modes [36]. In the present case, the modes are global, that is, for the entire stepped shaft. The characteristic equation is obtained from the determinant of the matrix $[G(\lambda)]$, which must be zero for non-trivial solutions to exist. The eigenvalues will have the form,

$$\lambda_i^k=\sigma_i^k\pm j\omega_i^k \quad \text{for } i=1,2,...;\ k=F,B; \tag{50}$$

where ω_i^k are the damped natural frequencies, σ_i^k are the damping parameters and F and B denote the forward and backward modes, respectively. In rotordynamics, the division between forward and backward modes is useful, as the latter case is generally avoided due to the stress distribution it generates along the shaft [37].

After obtaining the eigenvalues λ, the vibration modes of each segment can be obtained using Eqs. (33)-(36) together with Eqs. (45) and (49). The global functions will be piecewise continuous, and can be expressed as,

$$\phi_1(x)=\begin{cases}\phi_1^1(x) & \text{for } x_1<x<x_2\\ \phi_1^2(x) & \text{for } x_2<x<x_3\\ & \vdots\\ \phi_1^n(x) & \text{for } x_n<x<x_{n+1}\end{cases} \tag{51}$$

and the same form is true for $\phi_2(x)$, $\eta_1(x)$ and $\eta_2(x)$. These functions can be assembled by means of Eq. (19) to obtain the global vector $\{\Phi(x)\}$. With these global functions, one can solve the equations of motion for the generalized coordinates $q_i(t)$, as presented in Eq. (16). Note, however, that one actually needs the vector $\{\tilde{\Phi}(x)\}$, and not $\{\Phi(x)\}$, which was the vector obtained in this section. This is not really a problem, since the process to obtain $\{\tilde{\Phi}(x)\}$ is exactly the same, but one needs to change the matrices $[M]$ and $[K]$ for $[M]^H$ and $[K]^H$, respectively. After obtaining $\{\tilde{\Phi}(x)\}$ and solving Eq. (16), the physical displacements can be obtained from (13), which leads to,

$$u(x,t)=\sum_{i=1}^{\infty}\phi_1^{(i)}(x)q_i(t), \tag{52}$$

$$\psi(x,t)=\sum_{i=1}^{\infty}\eta_1^{(i)}(x)q_i(t), \tag{53}$$

where the functions $\phi_1^{(i)}$ and $\eta_1^{(i)}$ are global and the subscript $^{(i)}$ denotes here the ith mode; one must not be confused with the local segments of Eq. (51). In addition, the horizontal (y) and vertical (z) components are simply the real and imaginary parts of $u(x,t)$ and $\psi(x,t)$, respectively.

Here, the CSM is completely established, and it is an alternative to solve the problem of rotordynamics presented in the previous section. As far as the system considered (a rotor with a stepped shaft, concentrated disks and bearings), the solutions by the CSM are exact. It is important to note, however, that this does not limit the present approach, as the model can be applied to more complicated rotors, but the solutions would then be approximate rather than exact.

4. Results and discussion

This section presents some examples of the method proposed in some practical applications commonly seen in rotor dynamics, namely the obtention of natural frequencies and mode shapes, unbalance responses, and the behavior from nonlinear forces. In the latter case, the rotor-stator rubbing was studied. In all applications, an equivalent model based on the FEM is also developed for comparison. The results are obtained using the software Matlab. The natural frequencies in the CSM are obtained by means of the function *fsolve*, while in the FEM the *eig* function is used. In the unbalance response, both CSM and FEM models are solved analytically, while in the rubbing response, the *ode45* integrator is used in both cases.

4.1. Application 1: natural frequencies and mode shapes

In the first study, a simple uniform rotor is studied, with an off-centered disk and two bearings at the free ends, as depicted in Figure 2a. The system is divided into three segments: segment 1 and 3 have the same length $l_1 = 50$ mm and are where the bearings are located; segment 2 has $l = 500$ mm with a disk positioned at one-third of the shaft length or $a = 150$ mm in the local coordinate. The remaining parameters are listed in Table 1. The rotor was considered with short and long bearings. For short bearings, the coordinates $b_1 = b_2 = 25$ mm are used, meaning that the bearings are acting in the mid-span of the segment. The long bearings, however, act on the whole segments, similar to an elastic foundation.

To evaluate the CSM, FEM model was developed. Figure 2b shows the mesh used, which contains 24 finite elements with 4 degrees of freedom per node. The elements are standard Timoshenko beams with gyroscopic effect. The matrices used can be consulted in [32] or [38]. Similar to the CSM, the FEM rotor was considered with short and long bearings. In the former case, the bearing coefficients are simply summed in the stiffness and damping matrices at their corresponding degrees of freedom, which was in nodes 2 and 24. When long bearings were used, they were added at elements 1, 2, 23 and 24 as a distributed stiffness and damping. One is referred to [39] on how to introduce long bearings in the finite element rotor.

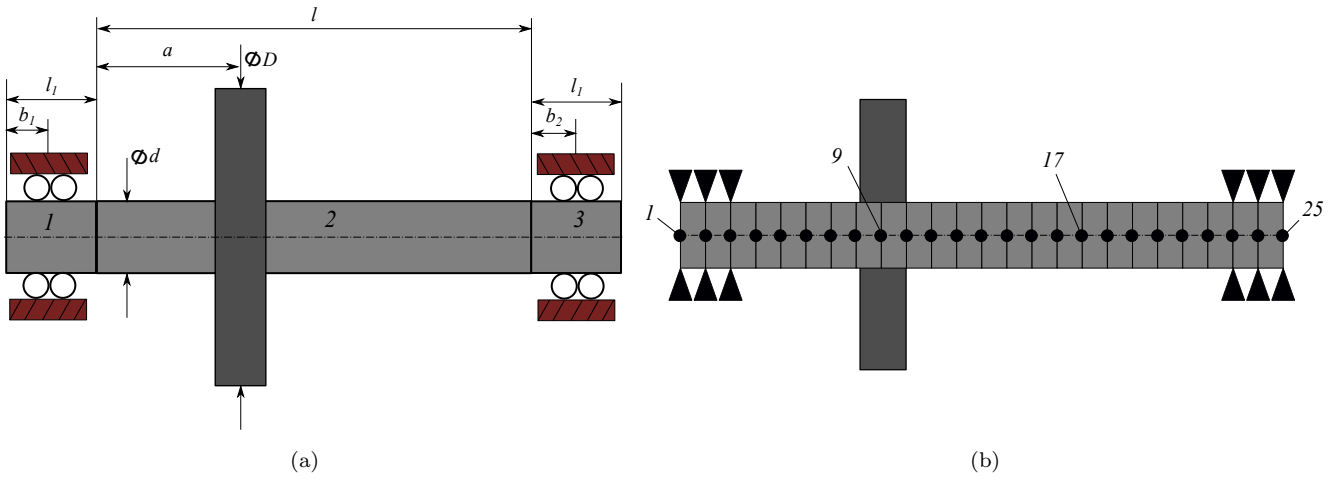

(a) (b)

Figure 2: Uniform rotor: (a) CSM dimensions and (b) finite element mesh.

Table 1: Parameters used in application 1.

Parameter	Value
Shaft's length	600 mm
Shaft's diameter	24 mm
Segments' 1 and 3 length	50 mm
Segment's 2 length	500 mm
Density	7850 kg/m^3
Elastic modulus	200 GPa
Poisson's ratio	0.3
Shear modulus	76.92 GPa
Shear factor	0.8864
Disk thickness	15 mm
Disk external diameter	150 mm
Disk location (a)	150 mm
Bearing locations (b_1, b_2)	25 mm 25 mm

In the following analysis, the bearings are considered anisotropic with no cross-coupled coefficients (that is, orthotropic bearings, with $k_{yz} = k_{zy} = c_{yz} = c_{zy} = 0$). The ratio between the horizontal and vertical stiffness are fixed as $k_{zz}/k_{yy} = 0.8$ and the damping is isotropic, or $c_{yy} = c_{zz}$. For the units to be consistent, given a bearing stiffness for the short bearing, the distributed stiffness used in the long bearing model will be the coefficient divided by the bearing length (which in the present case is $l_1 = 50$ mm).

Figures 3a and 3b show the Campbell diagram of the uniform rotor with short bearings for different bearing stiffness. This diagram represent the damped natural frequencies of the rotor with the increase of the shaft rotation Ω. In these figures and in the following ones, FW denotes the forward frequencies, which are the modes where the

Table 2: Rotational frequencies of the uniform rotor with short bearing for $c_{yy} = 10^2$ Ns/m and different stiffness.

Bearing Stiffness (N/m)	Rotational Frequency (rpm)									
		$\Omega = 0$			$\Omega = 5000$			$\Omega = 10000$		
	Mode	CSM	FEM	Error (%)	CSM	FEM	Error (%)	CSM	FEM	Error (%)
$k = 10^6$	1 BW	4212.4	4212.4	0.0000	4211.8	4211.8	0.0000	4209.99	4209.9	0.0001
	1 FW	4442.0	4442.0	0.0000	4442.0	4442.0	0.0001	4441.9	4441.9	0.0001
	2 BW	11565	11565	0.0004	11494	11494	0.0004	11303	11303	0.0004
	2 FW	12767	12767	0.0005	12810	12810	0.0005	12915	12915	0.0005
$k = 10^{10}$	1 BW	5872.6	5874.9	0.0380	5823.4	5823.4	0.0000	5770.4	5770.4	0.0001
	1 FW	5877.1	5874.9	0.0380	5924.7	5924.7	0.0000	5972.9	5973.0	0.0001
	2 BW	27473	27499	0.0935	26894	26894	0.0018	26222	26222	0.0016
	2 FW	27524	27499	0.0890	28037	28037	0.0022	28513	28514	0.0023

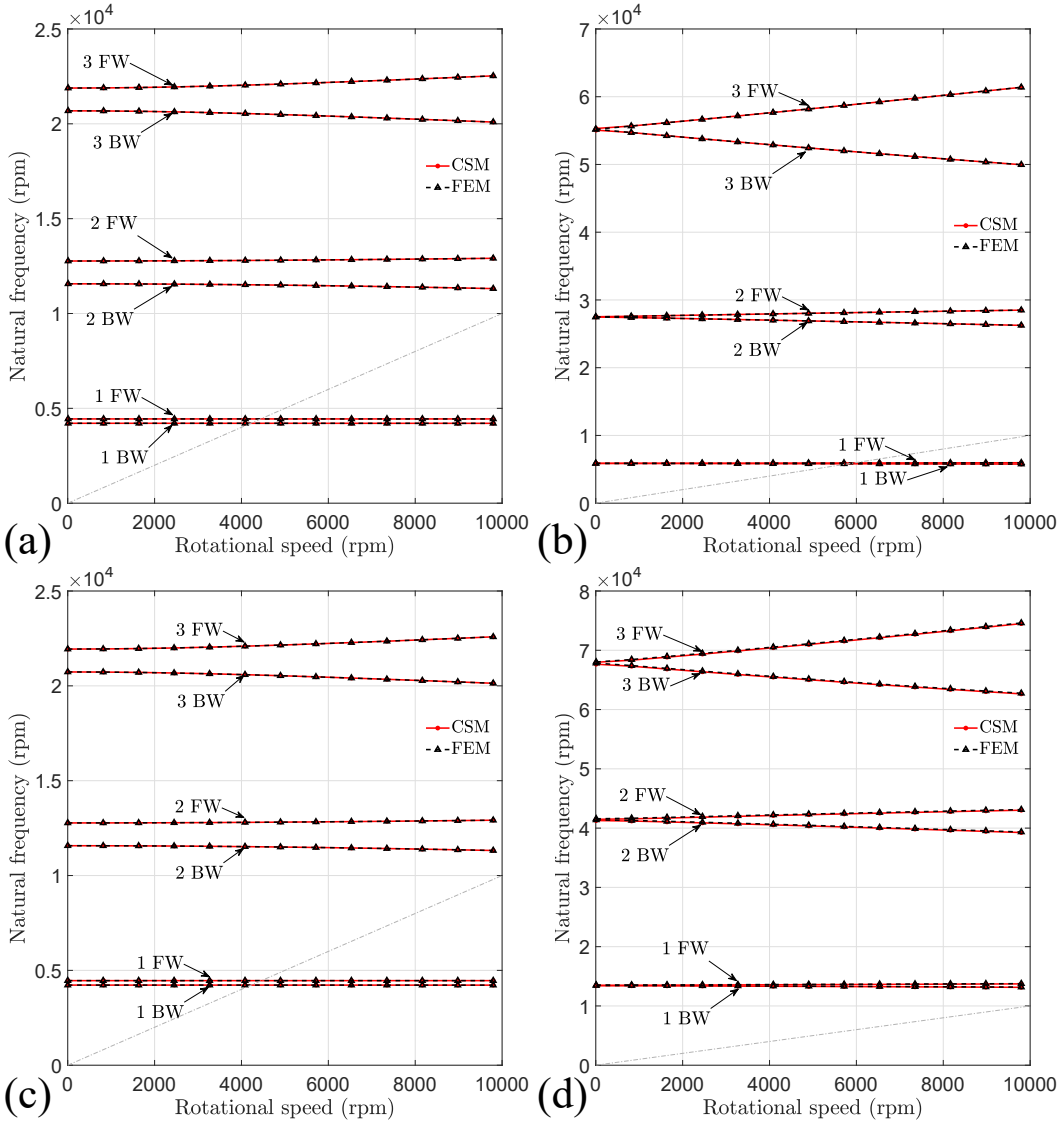

Figure 3: Damped natural frequencies of uniform rotor for $c_{yy} = 10^2$ and: (a) $k_{yy} = 10^6$ N/m (Short bearing), (b) $k_{yy} = 10^{10}$ N/m (Short bearing), (c) $k_{yy} = 10^6$ N/m (Long bearing), (d) $k_{yy} = 10^{10}$ N/m (Long bearing). The gray dashed line is where $\omega_n = \Omega$.

rotor whirls in the same direction as the shaft rotation; and BW denotes the backward frequencies, where the whirl is in the opposite direction of the rotation of the shaft. Since the rotor is anisotropic, the BW and FW frequencies will be different for the rotor at rest ($\Omega = 0$). The subsequent departure of the BW and FW modes is due to the gyroscopic effect. It is seen from Fig. 3 that the increase in the stiffness increases the natural frequencies, as expected, and the gyroscopic effect, since the difference between the FW and BW frequencies becomes greater. Table 2 shows some values extracted from the figures at certain speeds. The relative errors are calculated considering the frequencies of the finite element model as the exact value. As one can note from the figures and the low errors of the table, the agreement between the CSM and FEM is very good for the cases shown.

Similar as before, Fig. 3c and 3d shows the Campbell diagram for the uniform rotor with different bearing stiffness, but now with long bearings (Recall that for long bearings one has to divide the value by the length of the bearing,

Table 3: Rotational frequencies of the uniform rotor with long bearing for $c_{yy} = 10^2$ Ns/m and different stiffness.

Bearing Stiffness (N/m)	Rotational Frequency (rpm)									
		$\Omega = 0$			$\Omega = 5000$			$\Omega = 10000$		
	Model	CSM	FEM	Error (%)	CSM	FEM	Error (%)	CSM	FEM	Error (%)
$k = 10^6$	1 BW	4223.8	4223.8	0.0007	4223.2	4223.2	0.0007	4221.4	4221.4	0.0007
	1 FW	4458.8	4458.8	0.0008	4458.7	4458.8	0.0006	44586	44586	0.0006
	2 BW	11572	11572	0.0009	11501	11501	0.0003	11310	11311	0.0009
	2 FW	12773	12773	0.0011	12816	12816	0.0017	12921	12922	0.0010
$k = 10^{10}$	1 BW	13407	13446	0.2918	13291	13329	0.2817	13134	13170	0.2760
	1 FW	13487	13525	0.2804	13594	13634	0.2901	13725	13766	0.2947
	2 BW	41274	41384	0.2655	40350	40448	0.2420	39204	39299	0.2420
	2 FW	41484	41575	0.2186	42279	42381	0.2414	43046	43150	0.2413

$l_1 = 50$ mm). The results are very similar to the short bearing case seen before, the difference being only that now the frequencies are a bit higher. Table 3 shows some values taken from the Campbell diagram. For the rotor with long bearings, the errors between the CSM and FEM increase with the increase in the stiffness. However, they stay quite the same for the same stiffness and different rotational frequencies. The results show that, for the finite element mesh considered the CSM proved superior for rotors with long bearings, because they are better modeled as a continuous system due to their distributed nature.

Figure 4 shows the logarithmic decrement for the rotor with short and long bearings. In this case, the stiffness is fixed at $k_{yy} = 10^6$ N/m, and the damping is varied. The logarithmic decrement denotes the amount of damping in the system, and was calculated as $\delta = -2\pi Re[\lambda]/Im[\lambda]$, being λ the eigenvalue and $Re[\cdot]$ and $Im[\cdot]$ the real and imaginary parts, respectively. The parameter δ is also useful to detect instabilities in rotating machines. Comparing both damping cases, the backward modes appeared more damped then the forward ones, when higher damping is present. This is true only for modes 3 and 2, however, since the first mode showed almost no difference. With these results, the CSM shows similar damping to the FEM for either long or short bearings.

Lastly, the first undamped forward mode shape is shown in Figs. 5 and 6, for both types of bearings and different bearing stiffness. The mode shapes are normalized by the maximum displacement and the shaft rotation is set to $\Omega = 1000$ rpm. Since the bearings are anisotropic, the vertical and horizontal mode shapes can be different. For a bearing stiffness of $k_{yy} = 10^6$ N/m, the mode shapes of the rotor with short and long bearings look almost the same. For a higher bearing stiffness, however, this is not true, and the mode shapes start to look similar to a fixed-fixed end shaft for long bearings, while the short bearings makes the mode shapes look like a hinged support. It is also interesting to note that for higher stiffness, the vertical and horizontal mode shapes become almost identical, with minor differences. The results show that the CSM and FEM agree well for the mode shapes.

Here some aspects of the numerical simlations are discussed before moving on to the next application. The natural frequencies in the CSM are obtained from the determinant of $[G(\lambda)]$ in Eq. (49), which leads to transcendental equations. Such types of equations are more difficult to solve than the polynomial equations in the FEM. To obtain the Campbell diagrams, the natural frequency must be obtained in a wide range of speeds. Thus, in this regard, the

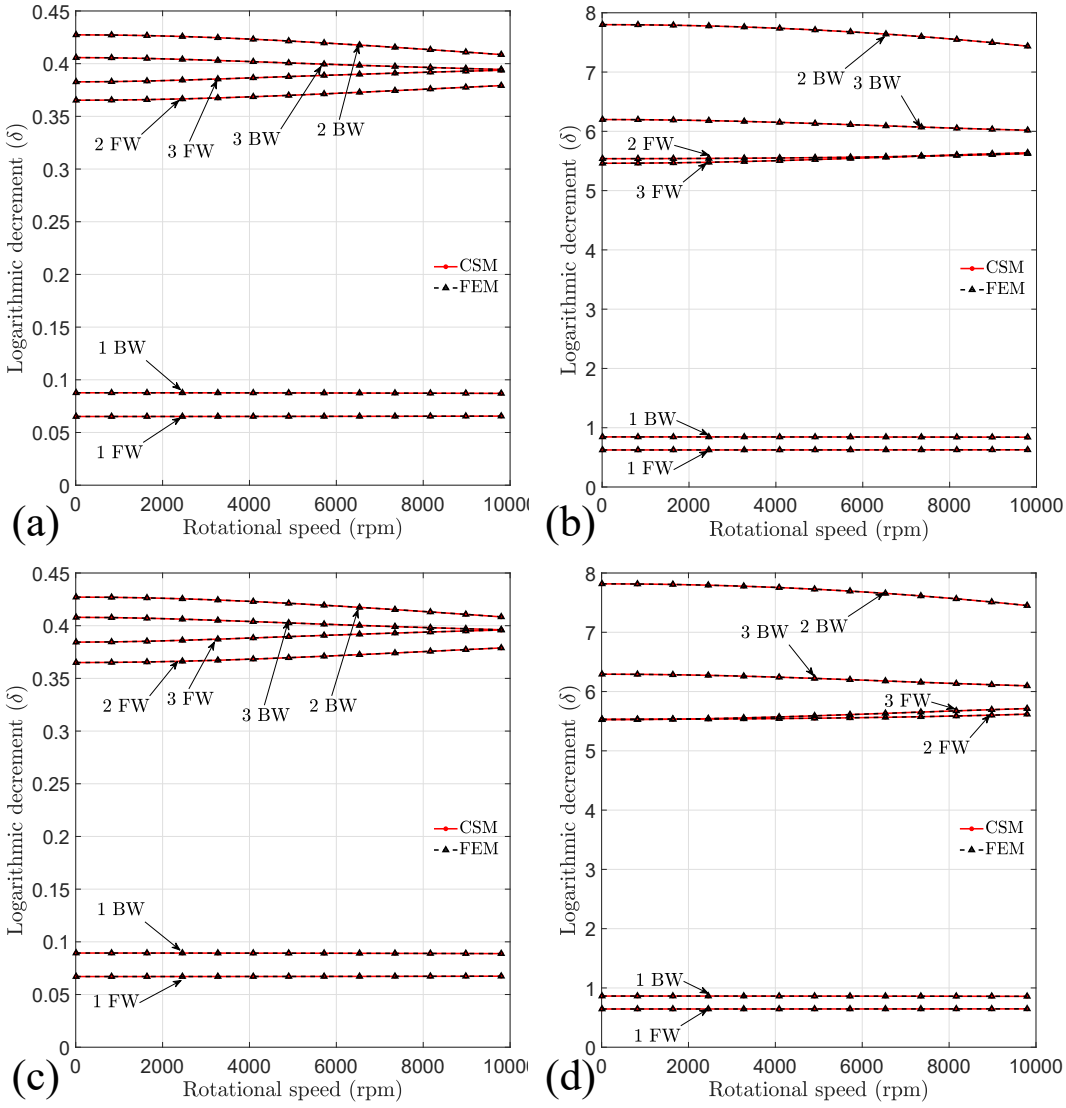

Figure 4: Logarithmic decrement of the uniform rotor with $k_{yy} = 10^6$ N/m and: (a) $c_{yy} = 10^2$ Ns/m (Short bearing), (b) $c_{yy} = 10^3$ Ns/m (Short bearing), (c) $c_{yy} = 10^2$ Ns/m (Long bearing) and (d) $c_{yy} = 10^3$ Ns/m (Long bearing).

CSM is in general slower then the FEM. For instance, using a laptop with an Intel i7-7500U processor, to obtain the results in Fig. 3, the CSM takes about ten seconds, while the FEM solution two to three seconds. In both methods, the frequencies were obtained for a total of 50 speeds, with equal spacing between the points. However, for high bearing stiffness, the mesh of the FEM must be refined to lower the errors between the CSM, and, for such a refined mesh, the solution time between the methods becomes similar, as the finite element matrices becomes very large. In the CSM, the addition of segments does not affect the results. This effect is more prominent in the rotor with long and stiff bearings. In the rotor with long bearings with $k = 10^{10}$ N/m, for example, in order for the errors of the FEM with respect to the CSM to go below 0.1 %, the mesh needs to be refined to have 48 elements (which is double the size of the mesh in Fig. 2b), and the computation time for 50 frequency steps becomes the same as the CSM. Therefore, the CSM proves to be a good alternative for rotors on stiff bearings, or when frequencies of higher modes are required.

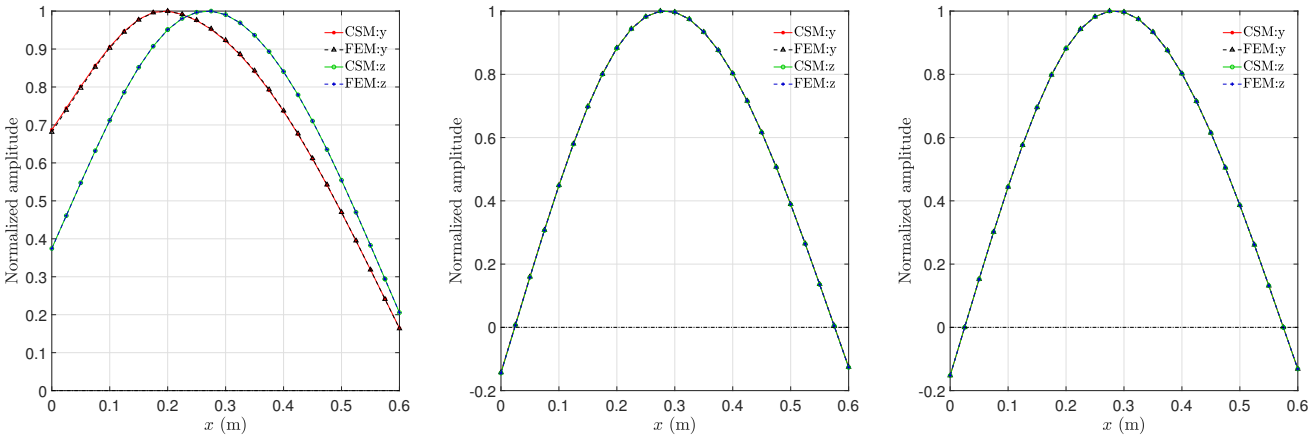

(a) (b) (c)

Figure 5: First undamped mode shape of the uniform rotor with short bearings for: (a) $k_{yy} = 10^6$ N/m, (b) $k_{yy} = 10^8$ N/m and (c) $k_{yy} = 10^{10}$ N/m.

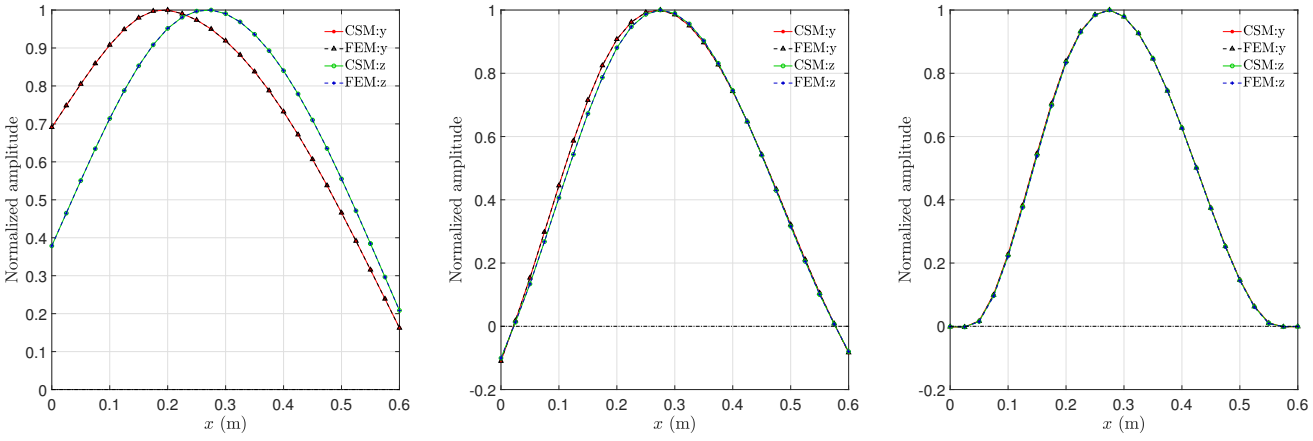

(a) (b) (c)

Figure 6: First undamped mode shape of the uniform rotor with long bearings for: (a) $k_{yy} = 10^6$ N/m, (b) $k_{yy} = 10^8$ N/m and (c) $k_{yy} = 10^{10}$ N/m.

4.2. Application 2: unbalance response

This example presents the application of the CSM to a multi-stepped rotor with several disks with the intention of obtaining its response to unbalance. The finite element mesh is presented in Fig. 7a, and it is based on a real turbo-machine. The rotor has a total length of $L = 2.5$ m, and the mesh consist of 26 finite elements considering rotary inertia and shear deformation. This is the baseline model, and will be denoted as FEM M1. Table 4 lists the lengths and diameters of the elements. The rotor has four disks positioned at nodes 12, 15, 17 and 19, and two bearings at nodes 6 and 23. Table 5 lists the diameters of the disks. The material considered was steel with the same density, Young's modulus and Poisson's ratio as the ones listed in Tab. 1 of the previous example. In addition, a less refined mesh was developed using the FEM, as shown in Fig. 7b and it is denoted as FEM M2. In this model, the

diameters of elements 1 and 2 are the mean diameters of elements 1 to 8 of FEM M1. Similarly, the last two elements' diameters are obtained from the mean of elements 21 to 26 of the mesh in Fig. 7a. The remaining mesh of FEM M2 is reduced to its minimum elements, given the location of the disks.

Two models based on the CSM were developed, they are shown in Figs. 7c and 7c, and are denoted CSM M1 and CSM M2, respectively. Although it is possible to use every element in the mesh as a continuous segment, the addition of segments in general increase the computation cost in the CSM to a higher degree than adding elements in the FEM. For model CSM M1, the system consisted of eight segments, and the coordinates of the disks and bearings,

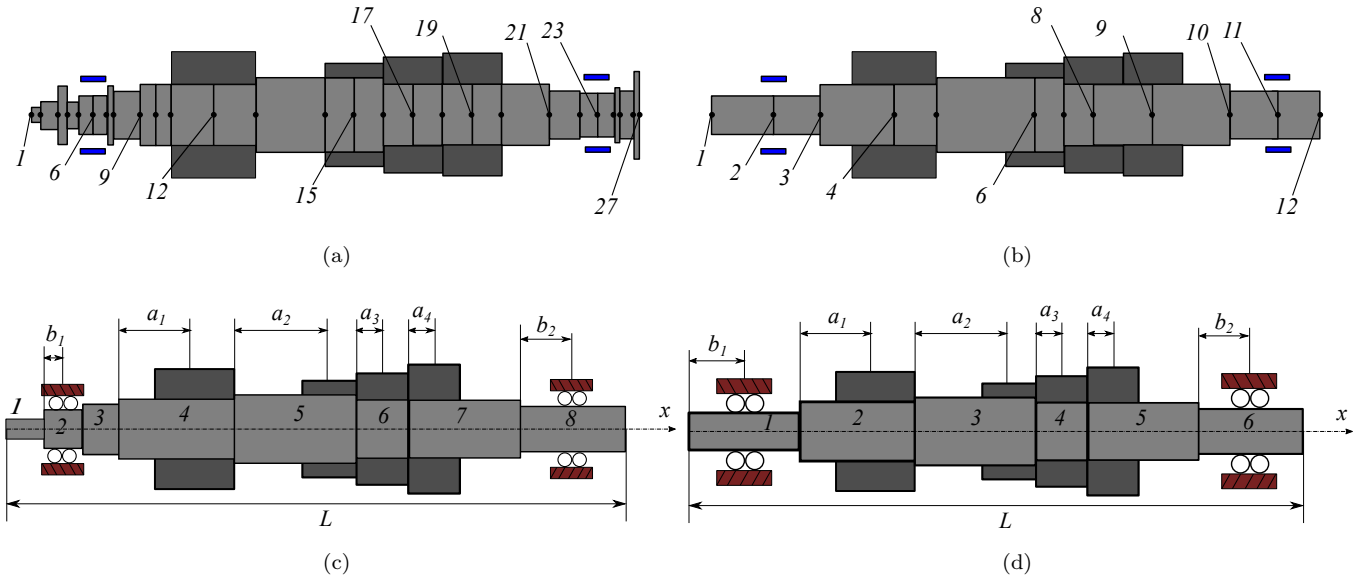

Figure 7: Models of the Multi-stepped rotor: (a) FEM M1, (b) FEM M2, (c) CSM M1 and (d) CSM M2.

Table 4: Finite element mesh data.

Element	Length (mm)	Diameter (mm)	Element	Length (mm)	Diameter (mm)
1	37.5	60	14	122	300
2	73.5	111.8	15	122	300
3	37.7	242	16	122	248
4	53.3	108.8	17	122	248
5	61	159.76	18	122	248
6	61	159.76	19	122	248
7	23.1	237	20	195.9	248
8	113.9	199.6	21	125	199.6
9	62.5	248	22	72.5	179.73
10	62.5	248	23	72.5	179.73
11	175.5	248	24	20	220
12	175.5	248	25	50	199.7
13	284	300	26	11	354

Table 5: Disks and bearings dimensions.

Parameter		Symbol	Value (mm)
	Position	a_1	300.5
Disk 1	Diameter	D_1	550
	Length	h_1	351
	Position	a_2	406
Disk 2	Diameter	D_2	350
	Length	h_2	244
	Position	a_3	122
Disk 3	Diameter	D_3	400
	Length	h_3	244
	Position	a_4	122
Disk 4	Diameter	D_4	450
	Length	h_4	244
Bearing 1	Position	b_1	61
Bearing 2	Position	b_2	197.5

listed in Tab. 5, were set based on their corresponding nodes in the finite element mesh. Segments 1, 2, 3, represent elements 1 through 8, and have diameters $d_1 = 108.8$ mm, $d_2 = 159.76$ mm and $d_3 = 199.6$ mm; while the lengths are $L_1 = 202$ mm, $L_2 = 122$ mm, $L_3 = 137$ mm. The lengths of segments 4, 5, 6, and 7 are $L_4 = 476$ mm, $L_5 = 528$ mm, $L_6 = 244$ mm and $L_7 = 439.9$ mm, and the diameters are the same as in the finite element model, that is, the diameters of elements 9 through 12, 13 through 15, 16 through 17 and 18 through 20, respectively. Segment 8 has a length of $L_8 = 351.1$ mm and a diameter of $d_8 = 222$ mm, which was obtained as the mean of the diameters 21 to 26 of the finite element mesh. The model CSM M2 has similar characteristics as the CSM M1, but segments 1 to 3 in the latter are transformed into a single segment, using the mean diameters of the finite element mesh from 1 to 8.

The purpose of all these different models based on FEM and CSM, is to evaluate what happens to their results as the mesh gets worsen. The model of Fig. 7a represents a highly discretized mesh, and the other models are alternative approaches to represent it with less computation.

Similar to the previous example, the rotor was considered with short and long bearings. For short bearings, the coordinates b_1 and b_2 are used in the CSM, while in the FEM they are placed in the corresponding nodes with bearings. When long bearings are used, the segment is considered on an elastic foundation, and in the finite element model, the elements have a distributed stiffness property. Also, segment 8 of CSM M1, and segments 1 and 6 of CSM M2, had to be further divided to include long bearings in them. The length of the bearings are $l_1 = 122$ mm and $l_2 = 145$ mm. Thus, the segments are divided such that the central sub-segments have the lengths aforementioned. Similarly, for the model FEM M2, two additional elements had to be included between elements 1 and 2 and 10 and 11, to place the distributed stiffness. The coefficients used in both CSM and FEM were:

$$\begin{bmatrix} k^1_{yy} & k^1_{yz} \\ k^1_{zy} & k^1_{zz} \end{bmatrix} = \begin{bmatrix} 2.66 & 5.80 \\ -6.93 & 1.53 \end{bmatrix} \times 10^8 \text{ N/m}, \quad \begin{bmatrix} k^2_{yy} & k^2_{yz} \\ k^2_{zy} & k^2_{zz} \end{bmatrix} = \begin{bmatrix} 2.35 & 8.88 \\ -9.47 & 1.24 \end{bmatrix} \times 10^8 \text{ N/m} \tag{54}$$

$$\begin{bmatrix} c^1_{yy} & c^1_{yz} \\ c^1_{zy} & c^1_{zz} \end{bmatrix} = \begin{bmatrix} 28.90 & -6.37 \\ -6.37 & 31.91 \end{bmatrix} \times 10^5 \text{ Ns/m}, \quad \begin{bmatrix} c^2_{yy} & c^2_{yz} \\ c^2_{zy} & c^2_{zz} \end{bmatrix} = \begin{bmatrix} 43.03 & -5.61 \\ -5.61 & 44.60 \end{bmatrix} \times 10^5 \text{ Ns/m} \tag{55}$$

where the superscripts denote the coefficients of bearings 1 (the left bearing) and 2 (the right bearing). These coefficients are obtained from a journal bearing using short bearing theory, considering a fluid viscosity of 0.028 Pa·s and a radial clearance of 90 μm. The coefficients can be consulted in [40], and the values were taken from a speed of $\Omega = 4000$ rpm. Although the coefficients are from short bearing theory, the same values were used for the long bearings, but the values were divided by the bearings lengths, which in this case were $l_1 = 122$ mm and $l_2 = 145$ mm.

To study the forced response of the rotor, an unbalance moment of $m_u e = 0.0213$ kg·m is placed at disk 2, at a coordinate $x_u = 1.343$ m from the left free end, or in node 15 in the mesh. To obtain the forced responses, three modes

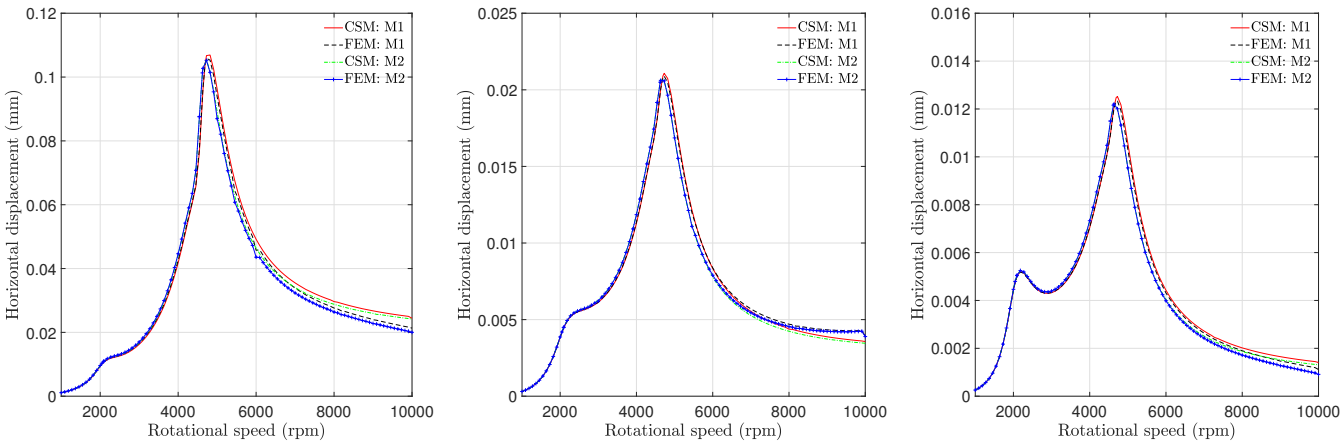

Figure 8: Unbalance response of the multi-stepped rotor with short bearings at: (a) Unbalance point, (b) bearing 1 and (c) bearing 2.

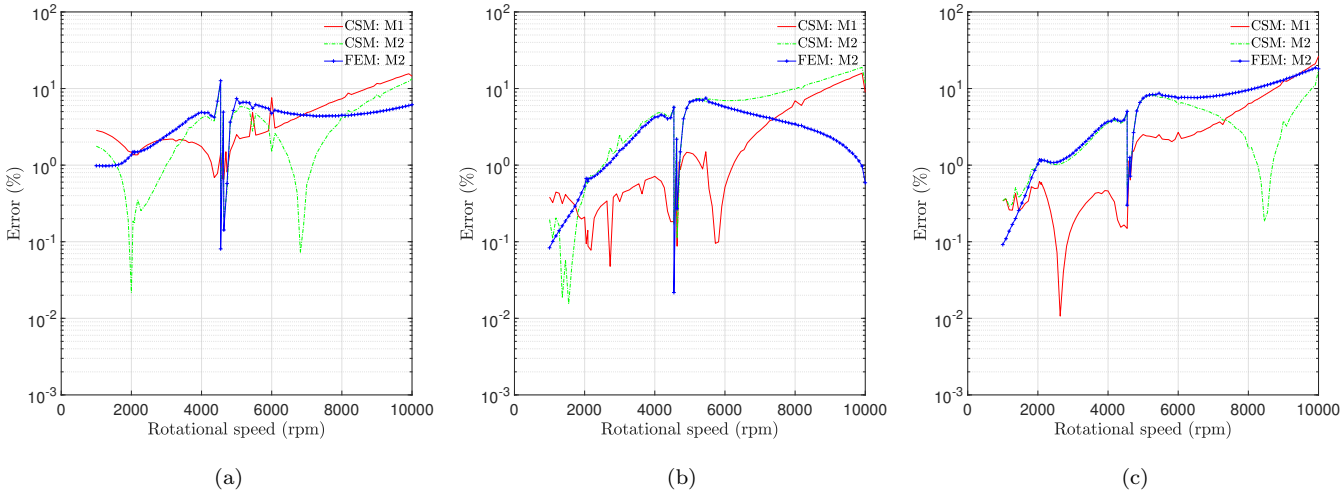

Figure 9: Errors in the amplitude relative to FEM M1, using short bearings, at: (a) Unbalance point, (b) bearing 1 and (c) bearing 2.

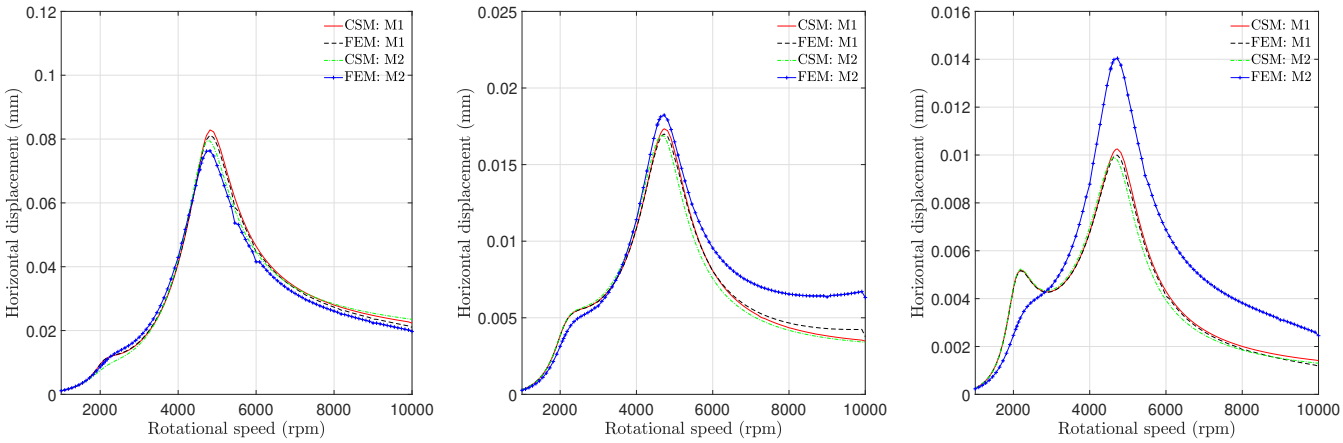

Figure 10: Unbalance response of the multi-stepped rotor with long bearings at: (a) Unbalance point, (b) bearing 1 and (c) bearing 2.

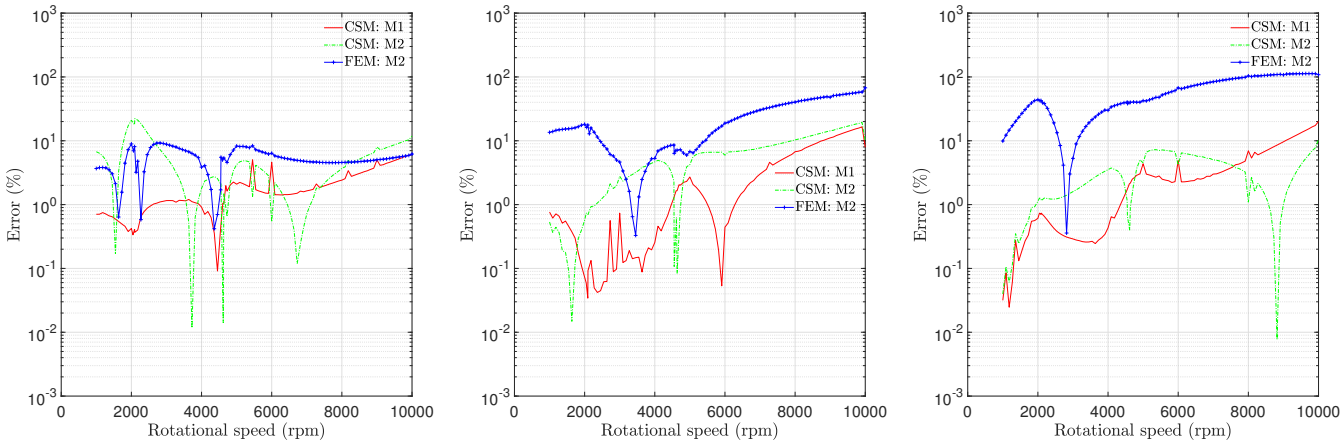

Figure 11: Errors in the amplitude relative to FEM M1, using long bearings, at: (a) Unbalance point, (b) bearing 1 and (c) bearing 2.

(three FW and three BW) were used in the CSM and all the degrees of freedom were considered in the FEM, that is, no reduction was performed. Figures 8 and 10 show the unbalance response at the bearings and unbalance point (disk 2) from 1000 to 10000 rpm using both types of bearings. The figure shows the displacements of all the models shown in Fig. 7. Additionally, Figures 9 and 11 show the errors in the amplitudes relative to FEM M1 (baseline). For short bearings, the responses are almost indistinguishable, as seen from the amplitudes and the low relative errors. The results for the rotor with long bearings were distinct for all models. The response closest to the baseline model was the CSM M1. In the second critical speed, one can note that the CSM showed a little higher displacement than the FEM, due to the difference in damping seen before. In addition, regarding the difference between the two types of bearings, the results agree with [39], where the long bearings showed more damping in general, and decreased the peak in amplitude at the critical speeds. This happens as the long bearings have a distributed damping, which have

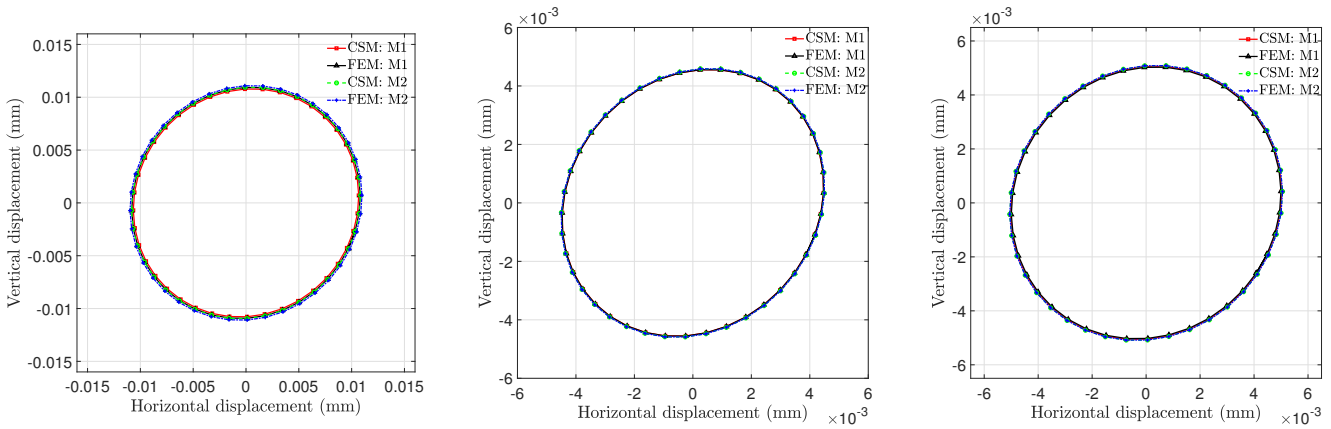

(a) (b) (c)

Figure 12: Obits of the rotor with short bearings at the first FW critical speed: (a) Unbalance point, (b) bearing 1 and (c) bearing 2.

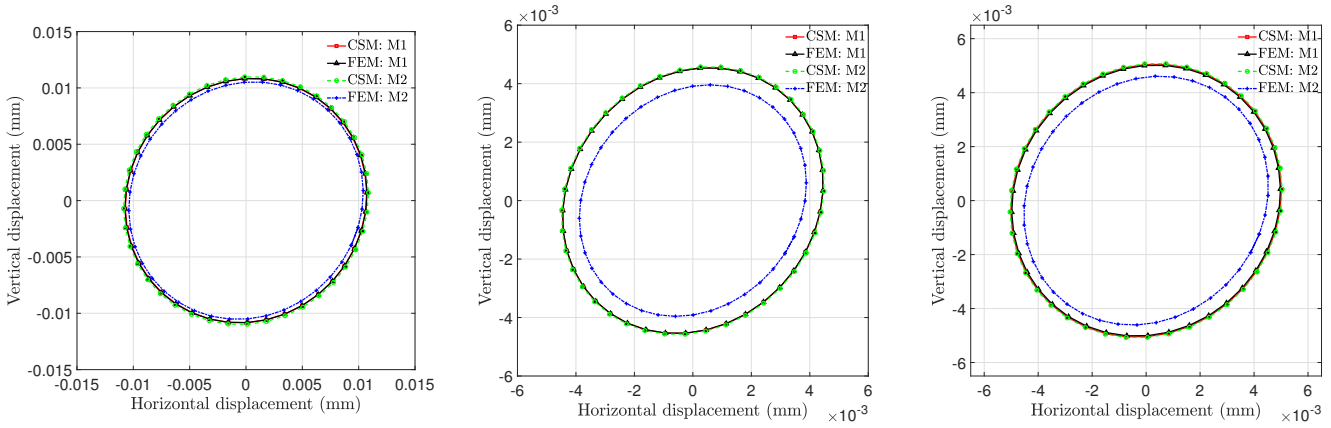

(a) (b) (c)

Figure 13: Obits of the rotor with long bearings at the first FW critical speed: (a) Unbalance point, (b) bearing 1 and (c) bearing 2.

a greater damping potential then the point-wise damping of the short bearing model. However, with regard to the natural frequencies, it was shown no difference between the two bearings.

Figures 12-15 show the orbits of the rotor at the same three locations, using both types of bearings and at the first two FW critical speeds. These speeds correspond to the peaks in Figs. 8 and 10. Just as before, the orbits for short bearings were similar for all models. For long bearings, the CSM M1 showed the best results, following by the CSM M2. The worst model was the FEM M2. The results presented in this section leads one to conclude that simplified models using the CSM can be more effective than rougher meshes using the FEM. Thus, when it comes to the reduction of the solution problem in rotor systems, the CSM proves to be a good alternative.

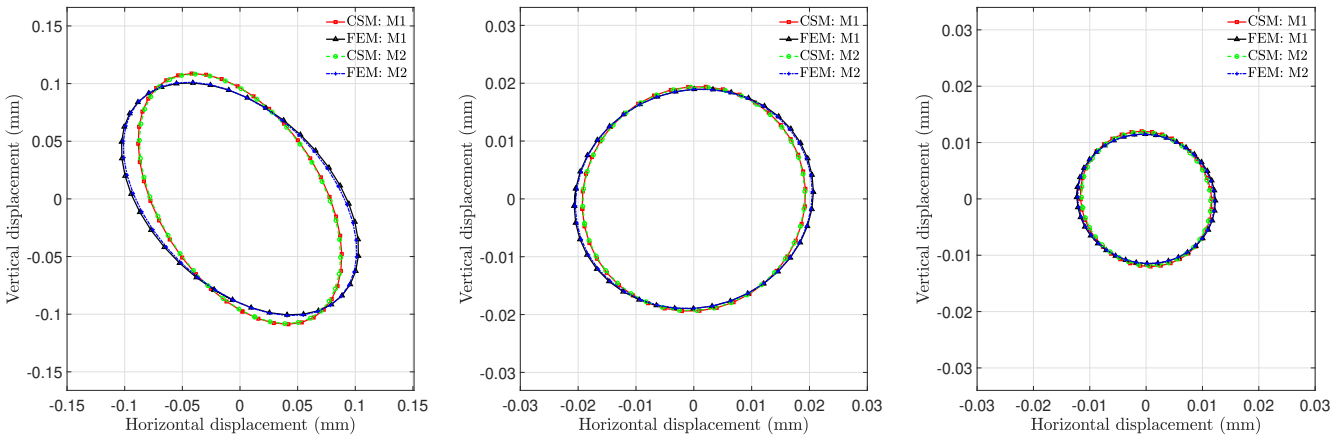

Figure 14: Obits of the rotor with short bearings at the second FW critical speed: (a) Unbalance point, (b) bearing 1 and (c) bearing 2.

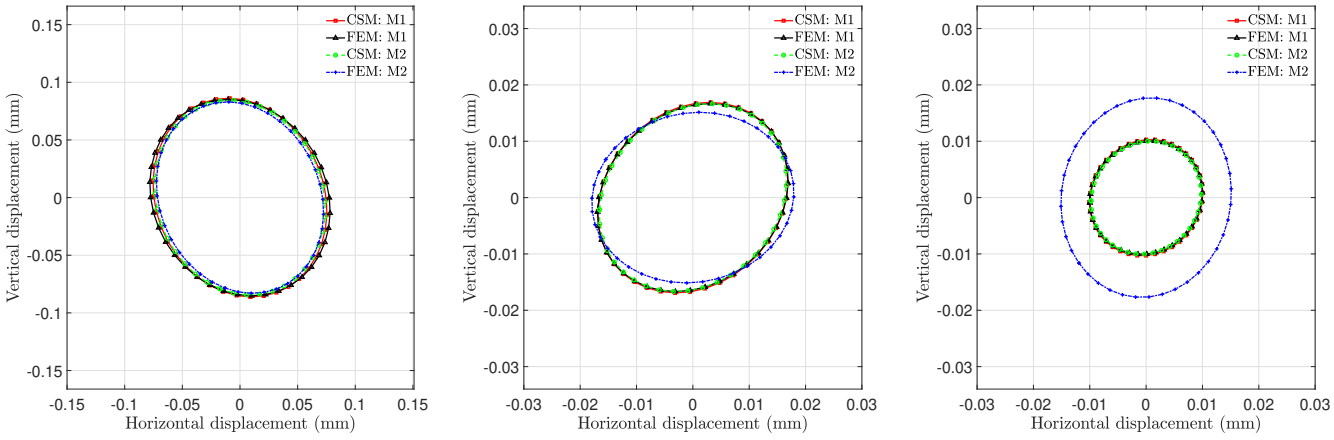

Figure 15: Obits of the rotor with long bearings at the second FW critical speed: (a) Unbalance point, (b) bearing 1 and (c) bearing 2.

4.3. Application 3: rotor-stator rubbing

Rotor-stator rubbing is a very important topic in rotordynamics. Since the gap between rotating and stationary part have been ever decreasing due to power requirements, it is a phenomenon that might always be present. Therefore, researchers and designers have been constantly trying to understand it, and many models have been employed in the literature. Some reviews on rubbing can be found in [41, 42].

Since the main objective here is to evaluate the CSM as an alternative for modeling rotors under nonlinear forces, the analysis will be simple. The same rotor presented in the first application is used, with dimensions and properties listed in Tab. 1. The unbalance moment is set to 0.37 kg·mm. The same bearings parameters are also considered: no cross-coupled coefficients, $k_{zz}/k_{yy} = 0.8$ and $c_{yy} = c_{zz}$. The values assumed were $k_{yy} = 10^8$ N/m and $c_{yy} = 10^4$ Ns/m. The impact model is the same as presented in [43, 44]. The parameters for the rubbing model are the impact

Table 6: Parameters used in the rotor-stator rubbing study.

Parameter	Value
Impact stiffness	10^7 N/m
Friction at contact	0.02
Radial clearance	0.2 mm
Rubbing axial location	0.3 mm (midspan)
Unbalance moment	0.37 kg·mm
Bearing stiffness	10^8 N/m
Bearing damping	10^4 Ns/m

stiffness, friction coefficient and gap distance between rotor and stator, which were set as 10^7 N/m, 0.02 and 0.2 mm, respectively. Also, the rubbing is considered to happen at the midspan of the shaft. The parameters used in the study are also listed in Tab. 6. In addition, since a comparison with the full FEM was already made in the previous section, here modal analysis (see [7]) was applied in the finite element's model. This is done in order to reduce the number of equations and to make a fair comparison with the CSM (which is a modal analysis, but with eigenfunctions instead of eigenvectors).

In order to analyze the rotor under rubbing, the following parameter $s = \Omega/\omega_{cr}$ was used, were ω_{cr} is the first forward critical speed. For the rotor with short and long bearings the critical speed is found to be $\omega_{cr} = 5910$ rpm and $\omega_{cr} = 8357$ rpm, respectively. For $s < 1$ one has a pre-resonance state, and for $s > 1$ a post-resonance state. Figures 16 and 17 shows the rubbing responses for the rotor on short bearings using the CSM and FEM for the first

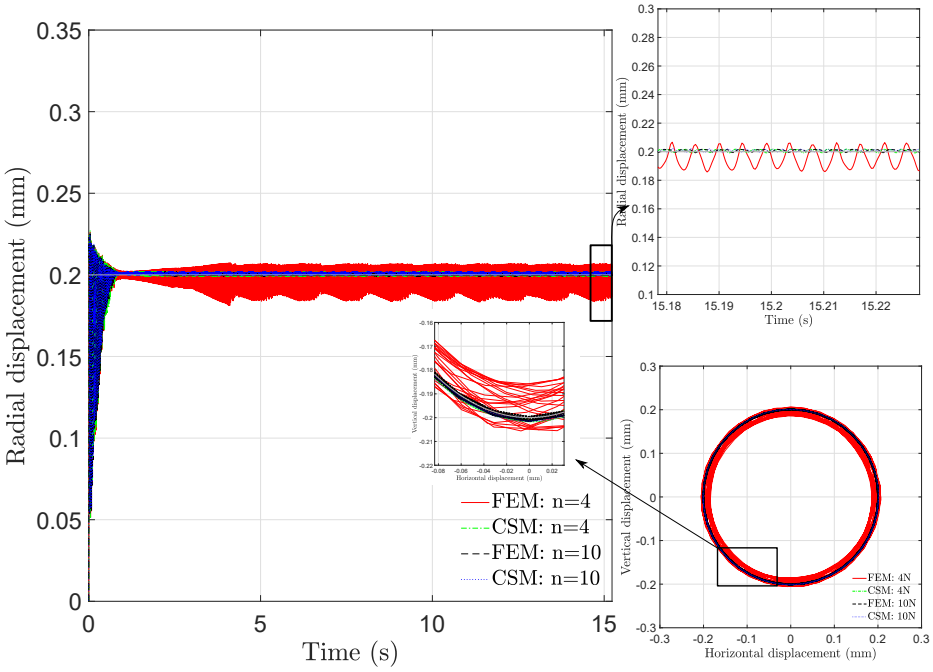

Figure 16: Rubbing response for the rotor on short bearings with $s = 0.8$. The gray line represents the radial clearance.

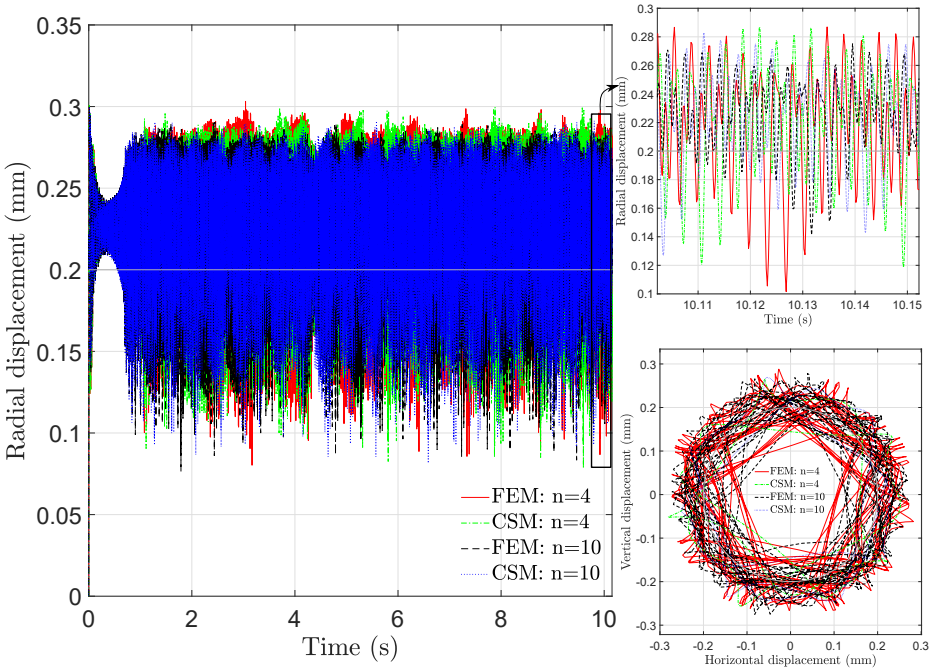

Figure 17: Rubbing response for the rotor on short bearings with $s = 1.2$.

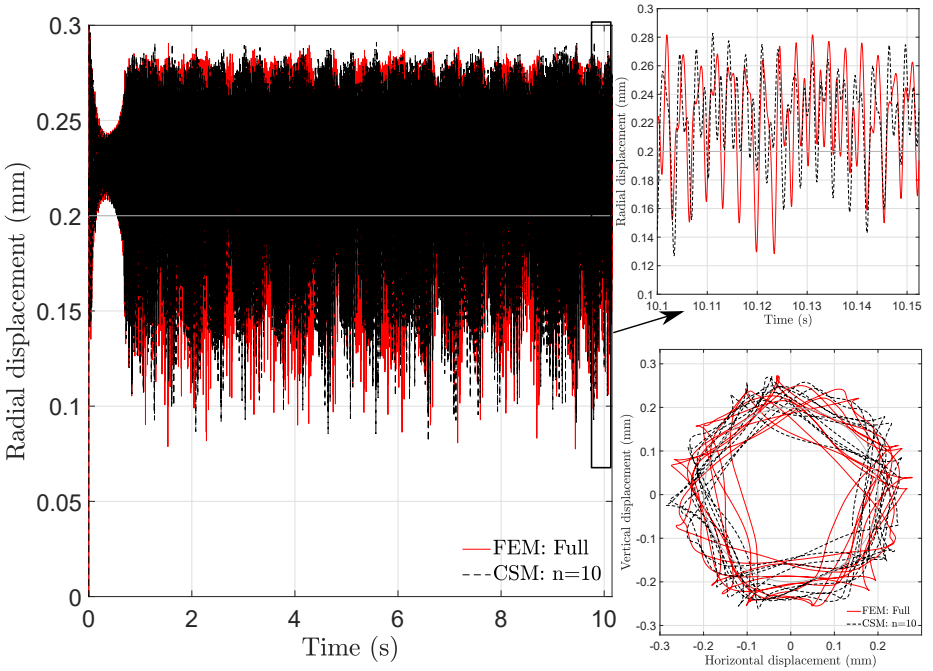

Figure 18: Comparison between the CSM with 10 modes and the full finite element method for the rotor on short bearings with $s = 1.2$.

1200 forcing cycles. The figures present the radial displacements and the rotor orbits during the rubbing phenomenon. To obtain these responses, modal analysis was performed, considering $n = 4$ and $n = 10$ natural modes (where half are forward modes and the other half backward modes). The speed was set to $s = 0.8$ and $s = 1.2$. From Fig. 16, one notes that the response using 4 modes with FEM was drastically different than using 10 modes. In contrast, 4 modes

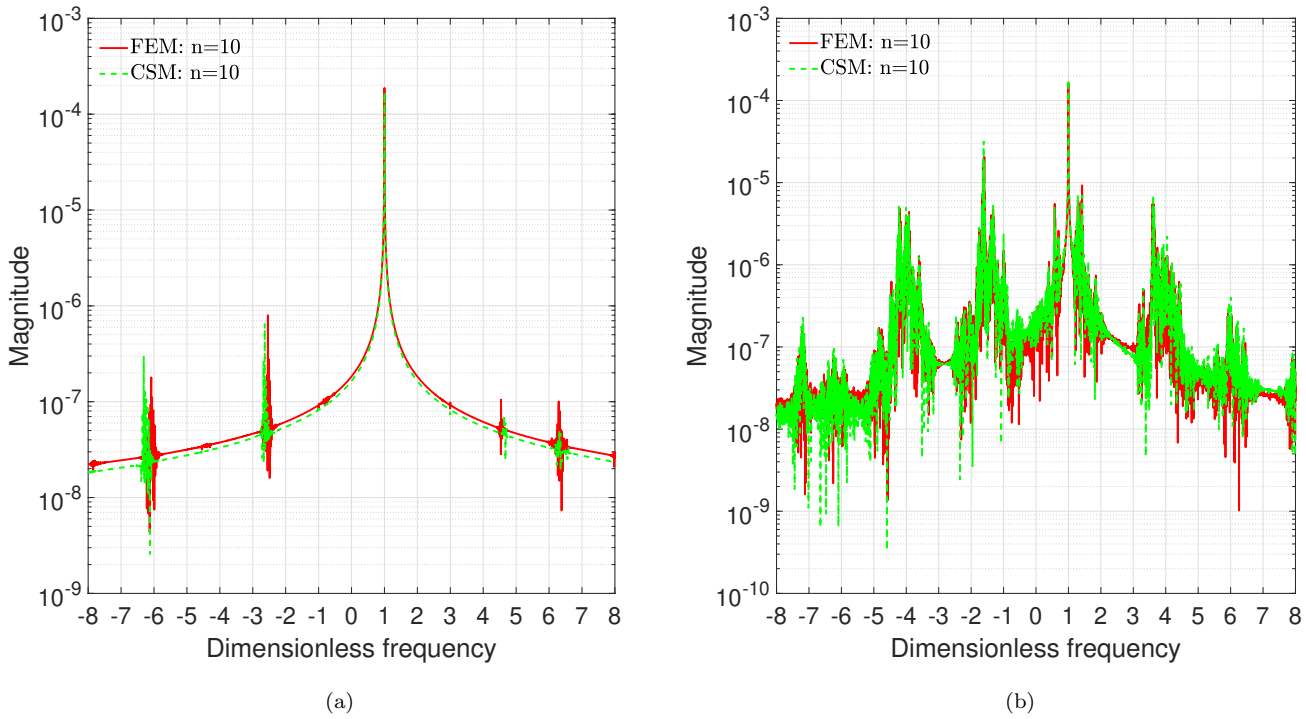

(a) (b)

Figure 19: Frequency spectrum normalized by the speed Ω of the rubbing response for the rotor on short bearings with: (a) $s = 0.8$ and (b) $s = 1.2$.

was already enough for the CSM to show very similar behavior to the response of the FEM with 10 modes. Figure 17 shows the responses when $s = 1.2$. The higher complexity of the dynamics is evident in this case. To test if 10 modes were enough with the CSM to represent the rubbing phenomenon, Figure 18 shows a comparison between the CSM with 10 modes and the integration of the full finite element equations, that is, with no modal analysis. Despite there being no exact resemblance between the CSM and full FEM, one can note a similar behavior in the responses. Also, this result validates the modal analysis applied in the finite element model in Figs. 16 and 17.

The double-sided frequency spectrum for the CSM and FEM with 10 modes are shown in Fig. 19. This figure is obtained by applying the Fast Fourier Transform (FFT) in the complex signal, $u_y + ju_z$, being u_y and u_z the horizontal and vertical displacement, respectively. The frequency is shown as a ratio of the speed Ω, and the negative and positive frequencies correspond to backward and forward components. The effect of the rubbing is clearly seen in the frequency domain by the multiple harmonics of the unbalance frequency, which is captured by both methods. One notes that the amplitude of the harmonics in the FEM and CSM are slightly different, which explains the difference seen in the time responses. Additionally, the agreement between the methods when $s = 1.2$ is better seen in the frequency domain, Fig. 19a, than the response in time, Fig 17. Therefore, whether the analysis is focused on the frequency spectrum or the displacement in time of the rotor, both the FEM and CSM can be used, as their results are similar with reasonable accuracy.

In Figs. 20 and 21, the rubbing response of the rotor with long bearings are shown. One may note, by comparing to the case with short bearings, that the rubbing appears less severe. This is due to the higher damping provided by

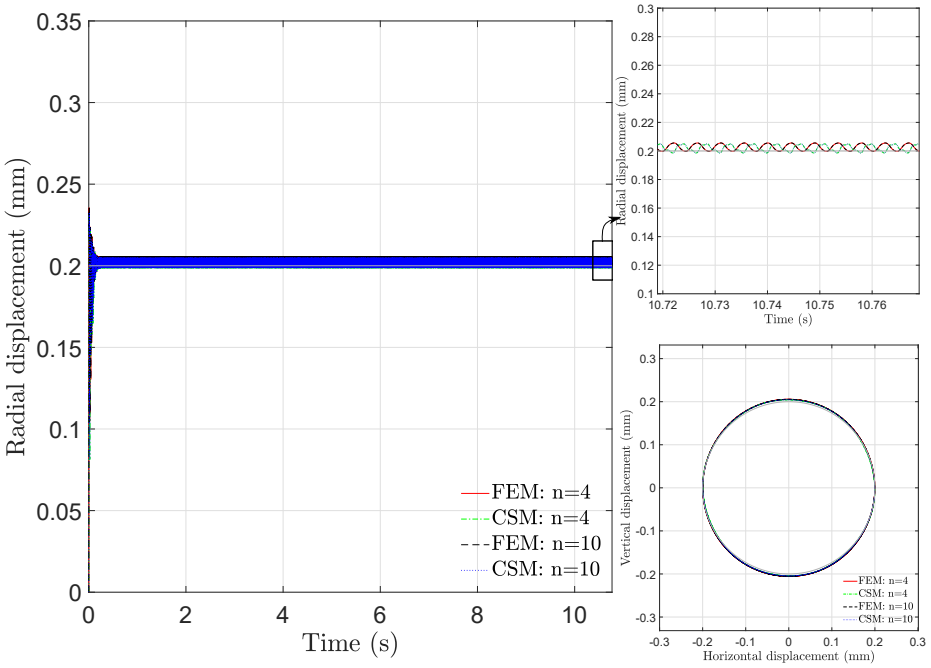

Figure 20: Rubbing response for the rotor on long bearings with $s = 0.8$.

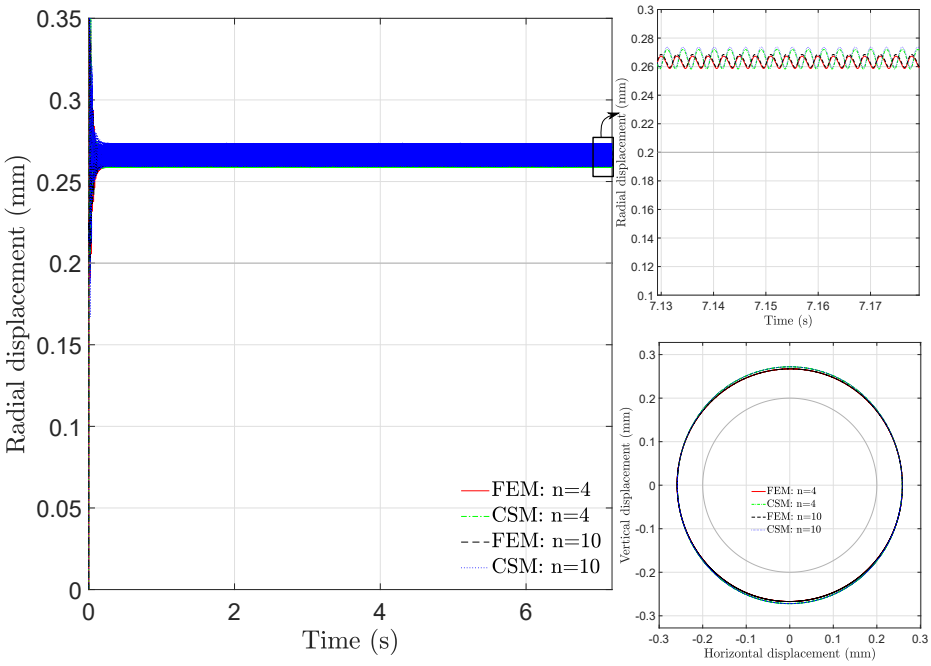

Figure 21: Rubbing response for the rotor on long bearings with $s = 1.2$.

the long bearing, as discussed in the previous section. The results of the CSM and FEM were also very similar for the rotor with rubbing and long bearings, as the figures show. In both speed operations, $s = 0.8$ and $s = 1.2$, using only 4 modes was already enough to simulate the rubbing. Additionally, Fig. 22 presents the response of the rotor in the frequency domain. Just as in the case of short bearings, the rubbing is seen by the appearance of multiple harmonics

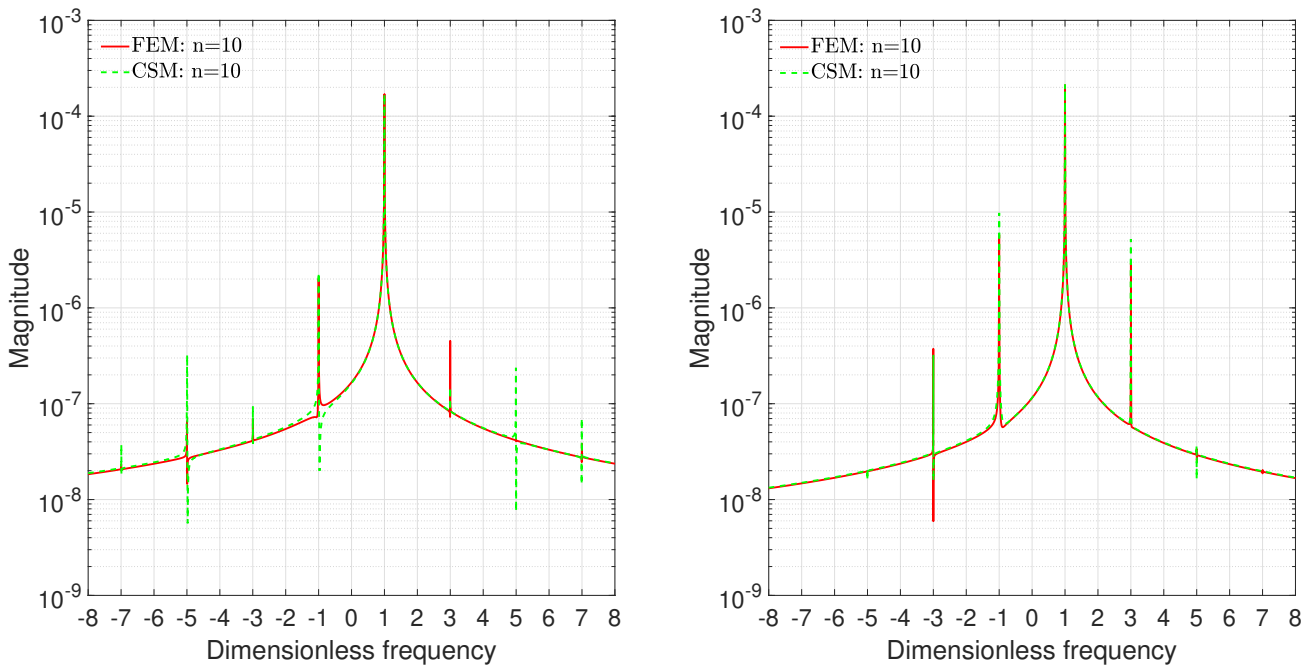

(a) (b)

Figure 22: Frequency spectrum normalized by the speed Ω of the rubbing response for the rotor on long bearings with: (a) $s = 0.8$ and (b) $s = 1.2$.

Table 7: Computation time for the rotor under rubbing.

Model	Fig. 16	Fig. 17	Fig. 20	Fig. 21
CSM ($n = 4$)	0.74 min	0.92 min	0.58 min	0.52 min
FEM ($n = 4$)	1.69 min	1.79 min	1.34 min	1.02 min
CSM ($n = 10$)	1.11 min	1.25 min	0.84 min	0.72 min
FEM ($n = 10$)	3.53 min	4.44 min	2.72 min	2.09 min

of the unbalance frequency. Here again, the amplitude of the harmonics differ by a small amount, which explains the little difference in the time responses.

The results above show the application of the proposed method for a rotor subjected to a nonlinear force. The comparison with the FEM shows good agreement, thus establishing the CSM as a viable alternative. Before continuing, it worth mentioning some aspects of the numerical simulation. In both methods, the results were obtained by means of the *ode45* integrator of Matlab. The equations of motion were placed in matrix form, and directly integrated. To apply the rubbing force, the Heaviside unit step function was used. In the CSM, the force location is set by defining the x coordinate in the modal vector $\{\tilde{\Phi}(x)\}$ (see Eq. (16)) by means of the Dirac's delta, while in the FEM the force is applied only at the specific node. Table 7 shows the computation time needed to obtain the results of Figs 16-21. These results are taken from the mean values of several runs, and the computer used was the same of the previous sections. The simulations for the rotor with long bearings took in general less time due to the higher damping. As

the table indicates, the CSM needed much less computational cost than the FEM. Therefore, the application of the CSM in nonlinear cases offers advantages in terms of numerical cost and shows similar accuracy when compared to the FEM.

5. Conclusions

The present paper expands the work presented in [28] and [27], in which a novel method, namely the CSM, to model multi-stepped rotor-bearings systems was introduced. The rotor can have several stepped sections, disks and bearings. The expansion presented here now allows the CSM to account for anisotropic bearings with either long or short characteristics.

In the CSM, the rotor system is modeled as beams with gyroscopic effect, rotary inertia and shear deformation taken into account. The method divides the system into segments, each with constant cross-section. Then, the eigenvalue problem of each segment is solved separately, and continuity conditions are applied to obtain the eigenfunctions and eigenvalues of the entire system. Due to the anisotropy, additional equations need to be solved, that take into account the shaft rotating in the opposite direction. After the eigenfunctions are obtained, modal analysis is applied to discretize the equations of motion, allowing the forced response to be obtained. The solutions given by the CSM can be considered exact for the system at hand (multi-stepped shaft modeled as 1D beam with disks and bearings), since no simplification is made in the equations of motion that lead to the eigenvalue problem. In that sense, any method that assumes a function to discretize the system will be an approximation, as in those cases the eigenvalue problem is simplified (if admissible functions are used), or avoided all together (if comparison functions are used)[11]. It is also worth noting that the CSM is mostly applicable when the rotating machine can be modeled as beams with lumped disks and bearings. If the model adopted is more complex, requiring 3D solid models, a 3D FEM method is the only tool available.

The evaluation of the method was done by means of the FEM for two systems: a uniform rotor and a multi-stepped rotor. The effects of bearings stiffness and damping were evaluated for the long and short bearings. The results consisted of Campbell diagrams, logarithmic decrements, mode shapes, unbalance response, and forced response under rubbing. Due to their distributed nature, long bearings were better modeled by the CSM, as the mesh in the FEM needs to be highly refined for the errors to reduce relative to the CSM, specially for stiffer bearings.

In the second numerical example, different models were established and compared to a baseline model. The idea was to evaluate the capacity of the CSM to reduce the full system and still presents reliable results. By comparing a FEM model with a rougher mesh with a reduced CSM model, the results showed that the latter is better to represent the full system. Since in many applications in rotating machinery a fast reliable solution is often needed, the CSM showed to be a good alternative to the FEM, and it can be used as an option to obtain reduced order models of rotors.

Lastly, the third application showed the use of the CSM and FEM to investigate the rotor-stator rubbing phenomenon. For that matter, the same rotor of the first example was used, with both long and short bearings. The results showed good agreement between the methods, and the CSM presented much less numerical cost as compared with the FEM. Thus, the proposed method proves a interesting alternative in the analysis of rotors under nonlinear forces.

Funding

The authors would like to thank CNPq (Grants #307941/2019-1 and #140275/2021-5) for the financial support to this research.

References

[1] U. Ehehalt, O. Alber, R. Markert, G. Wegener, Experimental observations on rotor-to-stator contact, Journal of Sound and Vibration 446 (2019) 453–467.

[2] N. Kushwaha, V. N. Patel, Modelling and analysis of a cracked rotor: a review of the literature and its implications, Archive of Applied Mechanics 90 (6) (2020) 1215–1245.

[3] H. D. Nelson, J. M. McVaugh, The Dynamics of Rotor-Bearing Systems Using Finite Elements, Journal of Engineering for Industry 98 (2) (1976) 593–600.

[4] Y. Briend, E. Chatelet, R. Dufour, M.-A. Andrianoely, F. Legrand, M. S. Sousa, V. Steffen, S. Baudin, Dry-whip phenomenon in on-board rotordynamics: Modelling and experimentation, Journal of Sound and Vibration (2021) 116398.

[5] H. Kim, E. Sikanen, J. Nerg, T. Sillanpää, J. T. Sopanen, Unbalanced Magnetic Pull Effects on Rotordynamics of a High-Speed Induction Generator Supported by Active Magnetic Bearings – Analysis and Experimental Verification, IEEE Access 8 (2020) 212361–212370.

[6] T. H. Machado, K. L. Cavalca, Investigation on an experimental approach to evaluate a wear model for hydrodynamic cylindrical bearings, Applied Mathematical Modelling 40 (21-22) (2016) 9546–9564.

[7] M. B. Wagner, A. Younan, P. Allaire, R. Cogill, Model reduction methods for rotor dynamic analysis: a survey and review, International Journal of Rotating Machinery 2010 (2010).

[8] T. J. R. Hughes, The finite element method: linear static and dynamic finite element analysis, Dover, 2000.

[9] K.-J. Bathe, Finite element procedures in engineering analysi., Prentice-Hall, 1982.

[10] J. M. Vance, B. Murphy, F. Zeidan, Machinery vibration and rotordynamics, Wiley, Hoboken, N.J, 2010.

[11] L. Meirovitch, Computational methods in structural dynamics, Vol. 5, Sjithoff & Noordhoff International Publishers, Rockville, USA, 1980.

[12] K. Torabi, H. Afshari, Exact solution for whirling analysis of axial-loaded Timoshenko rotor using basic functions, Engineering Solid Mechanics (2016) 97–108.

[13] S.-C. Hsieh, J.-H. Chen, A.-C. Lee, A modified transfer matrix method for the coupling lateral and torsional vibrations of symmetric rotor-bearing systems, Journal of Sound and Vibration 289 (1-2) (2006) 294–333.

[14] R. Bogacz, T. Szolc, H. Irretier, An Application of Torsional Wave Analysis to Turbogenerator Rotor Shaft Response, Journal of Vibration and Acoustics 114 (2) (1992) 149–153.

[15] H. Afshari, M. I. Rahaghi, Whirling analysis of multi-span multi-stepped rotating shafts, Journal of the Brazilian Society of Mechanical Sciences and Engineering 40 (9) (2018) 424.

[16] H. Afshari, K. Torabi, A. Jafarzadeh Jazi, Exact closed form solution for whirling analysis of Timoshenko rotors with multiple concentrated masses, Mechanics Based Design of Structures and Machines (2020) 1–24.

[17] O. S. Jun, J. O. Kim, Free bending vibration of a multi-step rotor, Journal of Sound and Vibration 224 (4) (1999) 625–642.

[18] S.-W. Hong, J.-H. Park, Dynamic analysis of multi-stepped, distributed parameter rotor-bearing systems, Journal of Sound and Vibration 227 (4) (1999) 769–785.

[19] O. Özcsahin, H. N. Özgüven, E. Budak, Analytical modeling of asymmetric multi-segment rotor–bearing systems with Timoshenko beam model including gyroscopic moments, Computers & Structures 144 (2014) 119–126.

[20] X. Tan, J. He, C. Xi, X. Deng, X. Xi, W. Chen, H. He, Dynamic modeling for rotor-bearing system with electromechanically coupled boundary conditions, Applied Mathematical Modelling 91 (2021) 280–296.

[21] C.-W. Lee, Y.-G. Jei, Modal analysis of continuous rotor-bearing systems, Journal of Sound and Vibration 126 (2) (1988) 345–361.

[22] C.-W. Lee, A complex modal testing theory for rotating machinery, Mechanical Systems and Signal Processing 5 (2) (1991) 119–137.

[23] G. Genta, A fast modal technique for the computation of the Campbell diagram of multi-degree-of-freedom rotors, Journal of Sound and Vibration 155 (3) (1992) 385–402.

[24] T. Szolc, On the Discrete–Continuous Modeling of Rotor Systems for the Analysis of Coupled Lateral Torsional Vibrations, International Journal of Rotating Machinery 6 (2000).

[25] A. C. Chasalevris, C. A. Papadopoulos, Nonlinear simulation of continuous rotor bearing systems with multi-step geometry, in: Proc. Of the 8th IFToMM Int. Conf. on Rotordynamics, Seoul, Korea, 2010.

[26] A. Chasalevris, C. Papadopoulos, A novel semi-analytical method for the dynamics of nonlinear rotor-bearing systems, Mechanism and Machine Theory 72 (2014) 39–59.

[27] A. Mereles, K. L. Cavalca, Mathematical modeling of continuous multi-stepped rotor-bearing systems, Applied Mathematical Modelling 90 (2021) 327–350.

[28] A. Mereles, K. L. Cavalca, Modeling of Multi-stepped Rotor-bearing Systems by the Continuous Segment Method, Applied Mathematical Modelling 96 (2021) 402–430.

[29] C. W. Lee, Vibration analysis of rotors, 1st Edition, Springer Science & Business Media, Dordrecht, Netherlands, 1993.

[30] L. B. Saint Martin, R. U. Mendes, K. L. Cavalca, Model reduction and dynamic matrices extraction from state-space representation applied to rotating machines, Mechanism and Machine Theory 149 (2020) 103804.

[31] G. Genta, Whirling of unsymmetrical rotors: A finite element approach based on complex co-ordinates, Journal of Sound and Vibration 124 (1) (1988) 27–53.

[32] M. I. Friswell, J. E. T. Penny, D. G. Seamus, A. W. Lees, Dynamics of rotating machines, Cambridge University Press, New York, 2010.

[33] G. Genta, Dynamics of rotating systems, Springer Science & Business Media, New York, 2007.

[34] H.-X. Li, C. Qi, Modeling of distributed parameter systems for applications—A synthesized review from time–space separation, Journal of Process Control 20 (8) (2010) 891–901.

[35] L. Meirovitch, L. Silverberg, Control of non-self-adjoint distributed-parameter systems, in: The 22nd IEEE Conference on Decision and Control, IEEE, 1983, pp. 281–285.

[36] S. S. Rao, Vibration of Continuous Systems, second edition Edition, John Wiley & Sons Ltd, 2019.

[37] A. Muszynska, Rotordynamics, Taylor & Francis, Boca Raton, 2005, oCLC: 839204137.

[38] R. Tiwari, Rotor Systems: Analysis and Identification, 1st Edition, CRC Press, Boca Raton, FL, 2017.

[39] A. S. Sekhar, B. S. Prabhu, Unbalance Response of Rotors Considering the Distributed Bearing Stiffness and Damping, in: International Gas Turbine and Aeroengine Congress and Exposition, The Hague, 1994.

[40] E. Krämer, Dynamics of rotors and foundations, Springer-Verlag Berlin Heidelberg GmbH, New York, 1993.

[41] G. Jacquet-Richardet, M. Torkhani, P. Cartraud, F. Thouverez, T. Nouri Baranger, M. Herran, C. Gibert, S. Baguet, P. Almeida, L. Peletan, Rotor to stator contacts in turbomachines. Review and application, Mechanical Systems and Signal Processing 40 (2) (2013) 401–420.

[42] K. Prabith, I. R. P. Krishna, The numerical modeling of rotor–stator rubbing in rotating machinery: a comprehensive review, Nonlinear Dynamics 101 (2) (2020) 1317–1363.

[43] M. Varanis, A. Mereles, A. Silva, J. M. Balthazar, A. M. Tusset, Rubbing Effect Analysis in a Continuous Rotor Model, in: K. L. Cavalca, H. I. Weber (Eds.), Proceedings of the 10th International Conference on Rotor Dynamics – IFToMM, Vol. 62, Springer International Publishing, 2019, pp. 387–399, series Title: Mechanisms and Machine Science.

[44] A. G. Mereles, K. L. Cavalca, On the analysis of a rotor system subjected to rub using a continuous model, in: 12th International Conference on Vibrations in Rotating Machinery, CRC press, London, 2020, p. 654.

[45] E. B. Magrab, Vibrations of elastic systems: With applications to MEMS and NEMS, Springer Netherlands, Dordrecht, Netherlands, 2012.

Appendix A. CSM functions

For a ith segment with a short bearing, the functions of the matrices $[C_i(\xi)]$, $[D_i(\xi)]$, $[E_i(\xi)]$ and $[F_i(\xi)]$, are:

$$\begin{cases} C_{ij}(\xi_i) = f_j(\xi_i) + \left[f_j(b_l)p_{1f}^{b_l}(\xi_i) + g_j(b_l)h_1^{b_l}(\xi_i)\right] H(\xi_i - b_l) \quad \text{for } j = 1,2,3,4; \\ C_{ij}(\xi_i) = f_j(b_l)p_{1b}^{b_l}(\xi_i)H(\xi_i - b_l) \quad \text{for } j = 5,6,7,8; \end{cases} \tag{A.1}$$

$$\begin{cases} D_{ij}(\xi_i) = g_j(\xi_i) + \left[f_j(b_l)p_{2f}^{b_l}(\xi_i) + g_j(b_l)h_2^{b_l}(\xi_i)\right] H(\xi_i - b_l) \quad \text{for } j = 1,2,3,4; \\ D_{ij}(\xi_i) = f_j(b_l)p_{2b}^{b_l}(\xi_i)H(\xi_i - b_l) \quad \text{for } j = 5,6,7,8; \end{cases} \tag{A.2}$$

$$\begin{cases} E_{ij}(\xi_i) = f_j(\xi_i) + \left[f_j(b_l)p_{3f}^{b_l}(\xi_i) + g_j(b_l)h_3^{b_l}(\xi_i)\right] H(\xi_i - b_l) \quad \text{for } j = 1,2,3,4; \\ E_{ij}(\xi_i) = f_j(b_l)p_{3b}^{b_l}(\xi_i)H(\xi_i - b_l) \quad \text{for } j = 5,6,7,8; \end{cases} \tag{A.3}$$

$$\begin{cases} F_{ij}(\xi_i) = f_j(\xi_i) + \left[f_j(b_l)p_{4f}^{b_l}(\xi_i) + g_j(b_l)h_4^{b_l}(\xi_i)\right] H(\xi_i - b_l) \quad \text{for } j = 1,2,3,4; \\ F_{ij}(\xi_i) = f_j(b_l)p_{4b}^{b_l}(\xi_i)H(\xi_i - b_l) \quad \text{for } j = 5,6,7,8; \end{cases} \tag{A.4}$$

If the segment has a disk, one has,

$$\begin{cases} C_{ji}(\xi_i) = f_j(\xi_i) + \left[f_j(a_k)p_1^{a_k}(\xi_i) + g_j(a_k)h_1^{a_k}(\xi_i)\right] H(\xi_i - a_k) \quad \text{for } j = 1,2,3,4 \\ C_{ij}(\xi_i) = 0 \quad \text{for } j = 5,6,7,8; \end{cases} \tag{A.5}$$

$$\begin{cases} D_{ji}(\xi_i) = g_j(\xi_i) + \left[f_j(a_k)p_2^{a_k}(\xi_i) + g_j(a_k)h_2^{a_k}(\xi_i)\right] H(\xi_i - a_k) \quad \text{for } j = 1,2,3,4 \\ D_{ij}(\xi_i) = 0 \quad \text{for } j = 5,6,7,8; \end{cases} \tag{A.6}$$

$$\begin{cases} E_{ji}(\xi_i) = C_{ji}^{-}(\xi_i) \;\; j = 1,2,\ldots,8; \\ F_{ji}(\xi_i) = D_{ji}^{-}(\xi_i) \;\; j = 1,2,\ldots,8; \end{cases} \tag{A.7}$$

For a segments with long bearings, one simply has,

$$\begin{cases} C_{ji}(\xi_i) = f_j(\xi_i) \;\; j = 1,2,\ldots,8; \\ D_{ji}(\xi_i) = g_j(\xi_i) \;\; j = 1,2,\ldots,8; \\ E_{ji}(\xi_i) = f_{j+8}(\xi_i) \;\; j = 1,2,\ldots,8; \\ F_{ji}(\xi_i) = g_{j+8}(\xi_i) \;\; j = 1,2,\ldots,8; \end{cases} \tag{A.8}$$

For an arbitrary segment i along the rotor with a kth disk and lth *short* bearing, the functions f_i, g_i $(i = 1,2,3,4)$, $p_{1,2}^{a_k}$ and $h_{1,2}^{a_k}$, are listed in [28]. The remaining functions are obtained as,

$$f_j(\xi_i) = f_{j-4}^{-}(\xi_i) \quad \text{for } j = 5,6,7,8 \tag{A.9}$$

$$g_j(\xi_i) = g_{j-4}^{-}(\xi_i) \quad \text{for } j = 5,6,7,8 \tag{A.10}$$

where $^{-}$ means interchanging Ω to $-\Omega$, that is, reversing the rotation direction. In addition, one has,

$$p_j^{a_k}(\xi_i) = p_{j-2}^{a_k,-}(\xi_i) \quad \text{for } j = 3,4 \tag{A.11}$$

$$h_j^{a_k}(\xi_i) = h_{j-2}^{a_k,-}(\xi_i) \quad \text{for } j = 3,4 \tag{A.12}$$

The functions, $p_{jf}^{b_l}$, $p_{jf}^{b_l}$, $p_{jb}^{b_l}$ and $p_{jb}^{b_l}$, for $j = 1, 2, 3, 4$, are given as,

$$p_{1f}^{b_l}(\xi_i) = \frac{k_f^l + \lambda c_f^l}{\kappa G A_i}\left[G_2^{b_l}(\xi_i) - \left(\frac{\rho A_i r_i^2}{EI_i}\left(\lambda^2 - 2j\lambda\Omega\right) + \frac{\kappa G A_i}{EI_i}\right) G_0^{b_l}(\xi_i)\right] \tag{A.13}$$

$$p_{2f}^{b_l}(\xi_i) = -\left(\frac{k_f^l + \lambda c_f^l}{EI_i}\right) G_1^{b_l}(\xi_i) \tag{A.14}$$

$$p_{3f}^{b_l}(\xi_i) = \frac{k_f^{l*} + \lambda c_f^{l*}}{\kappa G A_i}\left[G_2^{b_l,-}(\xi_i) - \left(\frac{\rho A_i r_i^2}{EI_i}\left(\lambda^2 + 2j\lambda\Omega\right) + \frac{\kappa G A_i}{EI_i}\right) G_0^{b_l,-}(\xi_i)\right] \tag{A.15}$$

$$p_{4f}^{b_l}(\xi_i) = -\left(\frac{k_f^{l*} + \lambda c_f^{l*}}{EI_i}\right) G_1^{b_l,-}(\xi_i) \tag{A.16}$$

$$p_{1b}^{b_l}(\xi_i) = \frac{k_b^l + \lambda c_b^l}{\kappa G A_i}\left[G_2^{b_l}(\xi_i) - \left(\frac{\rho A_i r_i^2}{EI_i}\left(\lambda^2 - 2j\lambda\Omega\right) + \frac{\kappa G A_i}{EI_i}\right) G_0^{b_l}(\xi_i)\right] \tag{A.17}$$

$$p_{2b}^{b_l}(\xi_i) = -\left(\frac{k_b^l + \lambda c_b^l}{EI_i}\right) G_1^{b_l}(\xi_i) \tag{A.18}$$

$$p_{3b}^{b_l}(\xi_i) = \frac{k_b^{l*} + \lambda c_b^{l*}}{\kappa G A_i}\left[G_2^{b_l,-}(\xi_i) - \left(\frac{\rho A_i r_i^2}{EI_i}\left(\lambda^2 + 2j\lambda\Omega\right) + \frac{\kappa G A_i}{EI_i}\right) G_0^{b_l,-}(\xi_i)\right] \tag{A.19}$$

$$p_{4b}^{b_l}(\xi_i) = -\left(\frac{k_f^{l*} + \lambda c_f^{l*}}{EI_i}\right) G_1^{b_l,-}(\xi_i) \tag{A.20}$$

Where the functions G_0, G_1 and G_2 are shown in [28].

For long bearings, the statement of the functions will not be productive due to their length. It is shown here the process required to obtain them instead. From the vector $\{b'\}$ in Eq. (31), one obtains several parameters multiplying the terms $\eta_1^i(0)$, $\phi_1^i(0)$, $\eta_2^i(0)$, and so on. The functions f, g, p and h, that appear in the matrices $[C_i(\xi)]$, $[D_i(\xi)]$, $[E_i(\xi)]$ and $[F_i(\xi)]$, comes from the inverse Laplace transform of these multiplying parameters. Consider, for example, the terms multiplying $\eta_1^i(0)$. To obtain $f_1(\xi_i)$, one needs to gather the parameters that multiply $\eta_1^i(0)$ in the first row of $\{b'\}$, and apply the inverse transformation. In the case of $f_1(\xi_i)$, one may have,

$$f_1(\xi_i) = \mathcal{L}^{-1}\left[\frac{C_1 s^6 + C_2 s^4 + C_3 s^2 + C_4}{(s^2 - \epsilon_{1i}^2)(s^2 - \epsilon_{2i}^2)(s^2 - \epsilon_{3i}^2)(s^2 - \epsilon_{4i}^2)}\right] \tag{A.21}$$

where C_j ($j = 1, 2, 3, 4$) are constants with the shaft properties. This transformation can be easily performed by means of tabulated data [45]. The transformations needed for the remaining functions are similar in nature to the above, and the whole process can be facilitated through the usage of a symbolic math software. Moreover, the following relations are valid for long bearings,

$$f_j(\xi_i) = f_{j-8}^-(\xi_i) \quad \text{for } j = 9, \ldots, 16 \tag{A.22}$$

$$g_j(\xi_i) = g_{j-8}^-(\xi_i) \quad \text{for } j = 9, \ldots, 16 \tag{A.23}$$

where, besides interchanging Ω with $-\Omega$, one needs also to change the bearing coefficients (k_f, c_f, k_b and c_b) by their complex conjugates (k_f^*, c_f^*, k_b^* and c_b^*).